

# Perturbation of boundary conditions to create appropriate ensembles for regional data assimilation in coastal estuary modeling

Yoshitaka Matsuzaki<sup>1</sup> and Tetsunori Inoue<sup>1</sup>

<sup>1</sup>Port and Airport Research Institute

November 24, 2022

## Abstract

Regional data assimilation is conducted for a coastal estuary using the ensemble Kalman filter, real observation data from Ise Bay, Japan, and a simulation model called the Ise Bay Simulator. The applicability and robustness of the method are then examined. We also analyze the relationship between the boundary conditions, which add perturbations and the data assimilation results of water temperature and salinity. A method of creating an ensemble by perturbing three boundary conditions (atmospheric forcing, lateral boundary conditions, river discharge forcing) is then proposed. In situ water temperature and salinity profiles observed at fixed points are assimilated daily. The proposed assimilation method provides stable data assimilation without unnatural values for water temperature and salinity throughout the year. Further, applying a perturbation to the three boundary conditions does not lead to filter divergence, thus indicating good applicability and robustness. Applying a perturbation to the three boundary conditions does not degenerate the ensemble spread. According to a sensitivity experiment, perturbing the atmospheric boundary conditions of air temperature and wind speed increases the ensemble spread of water temperature, especially near the surface layer. Wind speed has the greatest influence on the magnitude of the salinity ensemble spread, and its dominance depends on location. Perturbation of lateral boundary conditions increases the ensemble spread of water temperature and salinity at all water depths near the bay mouth, and the observations are effectively assimilated. Perturbation of river discharge forcing successfully assimilates water temperature and salinity near the estuary.

## Hosted file

essoar.10507831.1.docx available at <https://authorea.com/users/552408/articles/604741-perturbation-of-boundary-conditions-to-create-appropriate-ensembles-for-regional-data-assimilation-in-coastal-estuary-modeling>

1     **Perturbation of boundary conditions to create appropriate ensembles for regional**  
2                     **data assimilation in coastal estuary modeling**

3  
4     **Yoshitaka Matsuzaki<sup>1</sup> and Tetsunori Inoue<sup>1</sup>**

5     <sup>1</sup> Marine Environment Control System Department, Port and Airport Research Institute,  
6     Yokosuka, Japan

7  
8     Corresponding author: Yoshitaka Matsuzaki ([matsuzaki-y@p.mpat.go.jp](mailto:matsuzaki-y@p.mpat.go.jp))

9  
10    **Key Points:**

- 11       • This is the first study to apply the ensemble Kalman filter to an actual coastal estuary  
12       using real one-year observation data
- 13       • It is possible to maintain the ensemble spread by perturbing atmospheric forcing, lateral  
14       boundary conditions, and river discharge forcing
- 15       • This method achieves robust annual data assimilation and reflects seasonal fluctuations  
16

## 17 **Abstract**

18 Regional data assimilation is conducted for a coastal estuary using the ensemble Kalman filter,  
19 real observation data from Ise Bay, Japan, and a simulation model called the Ise Bay Simulator.  
20 The applicability and robustness of the method are then examined. We also analyze the  
21 relationship between the boundary conditions, which add perturbations and the data assimilation  
22 results of water temperature and salinity. A method of creating an ensemble by perturbing three  
23 boundary conditions (atmospheric forcing, lateral boundary conditions, river discharge forcing)  
24 is then proposed. In situ water temperature and salinity profiles observed at fixed points are  
25 assimilated daily. The proposed assimilation method provides stable data assimilation without  
26 unnatural values for water temperature and salinity throughout the year. Further, applying a  
27 perturbation to the three boundary conditions does not lead to filter divergence, thus indicating  
28 good applicability and robustness. Applying a perturbation to the three boundary conditions does  
29 not degenerate the ensemble spread. According to a sensitivity experiment, perturbing the  
30 atmospheric boundary conditions of air temperature and wind speed increases the ensemble  
31 spread of water temperature, especially near the surface layer. Wind speed has the greatest  
32 influence on the magnitude of the salinity ensemble spread, and its dominance depends on  
33 location. Perturbation of lateral boundary conditions increases the ensemble spread of water  
34 temperature and salinity at all water depths near the bay mouth, and the observations are  
35 effectively assimilated. Perturbation of river discharge forcing successfully assimilates water  
36 temperature and salinity near the estuary.

37

## 38 **Plain Language Summary**

39 The accuracy of numerical simulations of physical quantities such as water temperature and  
40 salinity in coastal estuaries may be hindered by limitations to set accurate calculation conditions.  
41 Therefore, data assimilation is used to integrate observed values into numerical simulations.  
42 However, despite progress in large-scale data assimilation (for example, in the open ocean),  
43 applying data assimilation to small-scale complex phenomena in coastal areas is lacking. In this  
44 study, we propose a data assimilation method for a coastal area; specifically, Ise Bay in Japan.  
45 For data assimilation, it is particularly important to set an appropriate coefficient (background  
46 error covariance) that determines how to incorporate the observed values into the numerical  
47 simulation. Among the various numerical simulation conditions, we hypothesize that the  
48 boundary conditions have a dominant effect on the error of the numerical simulation in coastal  
49 areas; therefore, we set the boundary conditions according to the magnitude of error. The data  
50 assimilation results for water temperature and salinity over one year exhibit high accuracy and  
51 verify the applicability and robustness of the proposed data assimilation method.

## 52 **1 Introduction**

53 There are certain difficulties in conducting precise numerical simulation of physical  
54 phenomena at coastal estuaries. Data assimilation methods can improve the reproduction  
55 accuracy and advance our understanding of physical processes. However, applying data  
56 assimilation to coastal numerical simulations is still challenging because of the complexity of the  
57 physical process (Stanev et al., 2016). One of the most important conditions of data assimilation  
58 is the background error covariance (forecast error covariance) (Edwards et al., 2015; Hoteit et al.,  
59 2018; Moore et al., 2011; Sakov et al., 2012). Although there are several methods for calculating

60 the background error covariance (Fisher & Courtier, 1995; Fu et al., 1993; Weaver & Courtier,  
61 2001), an appropriate method for regional data assimilation in coastal estuaries has not yet been  
62 determined. From this viewpoint, the ensemble Kalman filter (EnKF), which can express and  
63 update the background error covariance using ensemble members that indicate the system error,  
64 i.e., the numerical simulation error (Evensen, 1994), is a potential procedure for coastal  
65 calculation.

66 Ensemble members are created by perturbing the error factors of numerical simulations to  
67 represent the ensemble spread or variability. There are approximately three types of error factor  
68 that contribute to the error of a numerical simulation: (1) initial conditions, (2) forcing data, and  
69 (3) model equations and parameters (Turner et al., 2008). For numerical models of open oceans,  
70 which are relatively advanced in data assimilation, several studies have suggested calculating  
71 ensembles to represent the atmospheric forcing errors (Lima et al., 2019; Mirouze & Storto,  
72 2019; Penny et al., 2015; Sakov et al., 2012), parameter errors (Brankart et al., 2015), and their  
73 combinations (Baduru et al., 2019; Kwon et al., 2016; Sanikommu et al., 2020; Vandembulcke &  
74 Barth, 2015). This reflects the assumption that initial conditions, models, and atmospheric  
75 boundary conditions are important for the precise simulation of physical processes in the open  
76 ocean, which has a relatively large calculation area and long-term fluctuations.

77 However, the successful perturbation of error factors to generate ensembles has not yet  
78 been achieved for regional data assimilation in coastal estuaries. We suggest that perturbation of  
79 three boundary conditions is required to generate ensembles for regional data assimilation of a  
80 coastal estuary specifically, atmospheric forcing, lateral boundary conditions, and river discharge  
81 forcing. This is because coastal areas are more affected by boundary conditions because of the  
82 small calculation area. Moreover, it is very difficult to set accurate boundary conditions because  
83 of limitations of available data set, despite their substantial influence on the results of regional  
84 coastal numerical simulations. Previous studies have reported that error variability caused by the  
85 initial conditions decreases with time in coastal numerical models (Turner et al., 2008) because  
86 such models are dominated by relatively short-term fluctuations. Moreover, the error caused by  
87 the initial conditions can be maintained by multiplicative inflation (Anderson & Anderson, 1999;  
88 Whitaker & Hamill, 2012); however, this technique does not generate a consistent physical  
89 model (Sanikommu et al., 2020).

90 Some previous studies have conducted regional data assimilation for coastal estuaries  
91 using EnKF. For example, Turner et al. (2008) generated ensemble members for EnKF by  
92 perturbing atmospheric forcing, lateral boundary conditions, and river discharge forcing. They  
93 also proposed adding random noise with a normal distribution to the boundary conditions of the  
94 ensemble members as a method of perturbation. They applied this method to observing system  
95 simulation experiments (OSSEs) in Port Phillip Bay, Australia, using assimilated sea surface  
96 temperature (SST) data modified for satellite observations, and reported good prediction  
97 capability. Hoffman et al. (2012) also conducted OSSEs in Chesapeake Bay, USA. The  
98 assimilated data included fixed point water temperature, salinity, and SST, modified from in situ  
99 and satellite observations. They created ensembles by perturbing the initial conditions and wind  
100 via atmospheric forcing. Although they did not add perturbations to lateral boundary conditions  
101 and river discharge forcing, they noted it may be necessary to add perturbations to lateral  
102 boundary conditions and river discharge forcing for generating ensembles when data assimilation  
103 is conducted using real observation data. Furthermore, Khanarmuei et al. (2021) conducted twin  
104 experiments and OSSEs for the shallow estuary of Currimundi Lake, Australia. They perturbed

105 the lateral boundary condition of water level and river discharge, forcing to assimilate the  
106 observed values of water level and current velocity. They also revealed the importance of the  
107 combined perturbation of boundary conditions and assimilated observations. Thus, it is important  
108 to perturb the lateral boundary condition of water level when assimilating the observed value of  
109 water level, and to perturb river discharge forcing when assimilating the observed value of  
110 current velocity. However, real observation data were not included in their experiments and  
111 synthetic observation data were simulated numerically. In addition, the error factors were already  
112 known because the experiments were virtual.

113 Thus, we conducted the EnKF in the Ise Bay, Japan (it is coastal area including estuary,  
114 and same target simulation area in this study) using actual observed data (Matsuzaki & Inoue,  
115 2020). Ensembles were made to perturb lateral boundary condition of water temperature and  
116 river water temperature. The assimilation results were compared with the observed values, and it  
117 was confirmed that the water temperature improved. However, this study was conducted only in  
118 the summer, and the data assimilation performance and the robustness of the data assimilation  
119 method throughout the year have not been evaluated. Therefore, it is imperative to conduct  
120 assessment throughout the year to respond to seasonal fluctuations and confirm applicability and  
121 robustness of the methods (Turner et al., 2008).

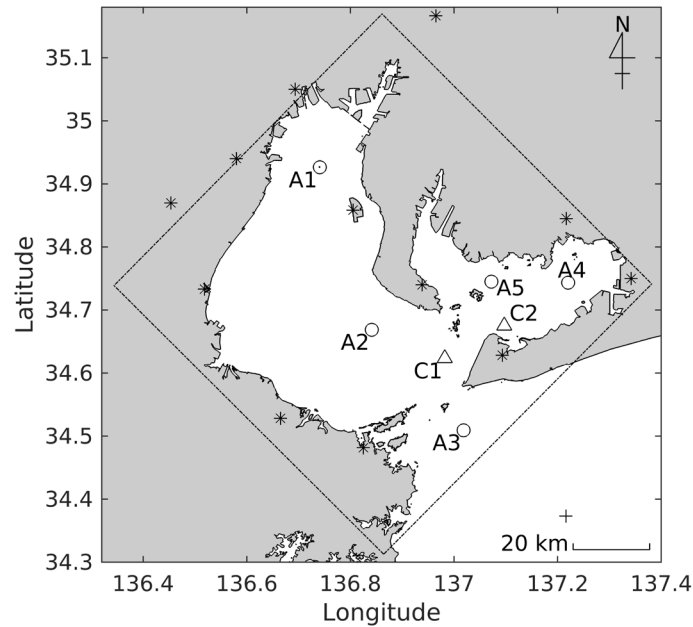
122 In this study, we conduct regional data assimilation for a coastal estuary using real  
123 observation data from Ise Bay, Japan, and evaluate the applicability of the data assimilation  
124 method. Specifically, we analyze the optimal method for adding perturbations to create ensemble  
125 members for regional data assimilation of a coastal estuary. This study also analyzes the  
126 relationship between the boundary conditions, which add perturbations and the assimilated water  
127 temperature and salinity data results as well as their ensemble spread. To the best of our  
128 knowledge, this is the first study to employ EnKF with actual water temperature and salinity data  
129 for a coastal estuary over one year. Additionally, no previous studies have generated ensembles  
130 by perturbing lateral boundary conditions and river discharge forcing under practical conditions;  
131 thus, this study reveals the effect of perturbing boundary conditions. In addition, we confirm the  
132 robustness of the regional coastal data assimilation method by performing long-term integral data  
133 assimilation and quantitative evaluation using the data assimilation results. The proposed data  
134 assimilation method is characterized by high applicability to coastal estuaries and responds to  
135 both short-term and long-term fluctuations, including seasonal changes.

## 136 **2 Materials and Methods**

### 137 **2.1 Simulation model and setup**

138 Simulations were conducted using the Ise Bay Simulator (Tanaka & Suzuki, 2010),  
139 which is a non-hydrostatic numerical simulation model. The model was configured to cover the  
140 entire area of Ise Bay (Figure 1, surface area: 2,342 km<sup>2</sup>, mean depth: 17 m, volume: 3.94×10<sup>10</sup>  
141 m<sup>3</sup>), which is located in the south-central part of Honshu Island, Japan. The bay is approximately  
142 70 km long in both longitudinal and latitudinal directions and is divided into two. The western  
143 side has a surface area of 1,738 km<sup>2</sup>, a mean depth of 20 m, and a volume of 3.39×10<sup>10</sup> m<sup>3</sup>. The  
144 eastern side is called Mikawa Bay, which has a surface area, mean depth, and volume of 604  
145 km<sup>2</sup>, 9 m, and 5.5×10<sup>9</sup> m<sup>3</sup>, respectively. The lateral boundary borders the Pacific Ocean. The Ise  
146 Bay model uses the cartesian coordinate system, which simulates the water current structure of  
147 coastal estuaries with a high horizontal resolution of 800 m. The coordinate system is set by

148 rotating it counterclockwise by  $45^\circ$ . The number of vertical layers is 32, with 0.5-m spacing near  
 149 the water surface and 30-m spacing near the seabed. Input water depth data were created by  
 150 reading the water depth from a chart made by the Japan Coast Guard. A subgrid-scale model was  
 151 used for the horizontal turbulence model; the model of Nakamura and Hayakawa (1991), which  
 152 has been modified from the model of Henderson-Sellers (1985), was used for the vertical  
 153 turbulence model. The Sommerfeld radiation condition was applied for the transmission  
 154 condition of the lateral boundary (Orlanski, 1976).



155

156 **Figure 1.** Location of Ise Bay, Japan. Dashed line indicates the experimental area for data  
 157 assimilation. Circles and triangles represent observation stations used for data assimilation and  
 158 accuracy validation, respectively. Asterisks represent the observation stations used to generate  
 159 atmospheric forcing data. Crosses represent the observation points used to generate the lateral  
 160 boundary conditions.

## 161 2.2 Boundary condition settings

162 This simulation system, which includes data assimilation, is designed from the  
 163 perspective of short-term forecasts. Therefore, the data used for the boundary conditions were  
 164 created using only data available in real time. Thus, more accurate data were not used for  
 165 boundary conditions unless they could be obtained in real time. Thus, although a system that  
 166 uses the output of an atmospheric simulation model as a boundary condition has since been  
 167 developed for this numerical simulation model (Hafeez et al., 2021; Matsuzaki et al., 2021), this  
 168 study adopted a system that creates boundary conditions based on observed values.

### 169 2.2.1 Atmospheric forcing

170 Atmospheric forcing data were generated from observation data from 12 terrestrial  
 171 observation stations of the Automated Meteorological Data Acquisition System (AMeDAS) near  
 172 Ise Bay (Nagoya, Centrair, Gamagori, Minamichita, Toyohashi, Irigo, Kuwana, Yokkaichi,  
 173 Kameyama, Tsu, Omata, and Toba). All atmospheric forcing data at each calculation grid were

174 interpolated using weighting interpolation with a normal distribution (the variance was 100 km<sup>2</sup>)  
 175 according to the distance from the observation stations. Shortwave radiation was calculated from  
 176 daylight hours following the method of Nimiya et al. (1997). Longwave radiation was calculated  
 177 according to the method of Nimiya et al. (1996). Wind velocity was set as follows. The observed  
 178 wind speed was converted to wind speed at an altitude of 100 m using the logarithmic law in  
 179 Equations (1) and (2):

$$W = \frac{U^*}{\kappa} \ln \frac{Z}{Z_0} \quad (1)$$

$$U^* = \frac{W_0 \cdot \kappa}{\ln \frac{h_m}{Z_0}} \quad (2)$$

182 where  $W$  is the converted wind speed,  $U^*$  is the friction speed,  $\kappa$  is the Kalman constant ( $\kappa = 0.4$ ),  
 183  $Z$  is the height from the bottom,  $Z_0$  is the roughness length,  $W_0$  is the wind speed at the  
 184 observation station, and  $h_m$  is the altitude of the wind anemometer. The roughness length at the  
 185 sea surface was set to 0.001 m, and the roughness length at each observation station was set  
 186 according to the work of Kuwagata and Kondo (1990). Wind velocity at each calculation grid  
 187 was interpolated using the same method as that for other weather data. Then, the wind speed at  
 188 an altitude of 10 m was obtained by Equation (1). Vapor pressure  $e$  [hPa] was calculated using  
 189 Equation (3) and (4):

$$e = es \times U/100 \quad (3)$$

$$es = 6.112 \times \exp\left(\frac{17.62T_a}{243.12+T_a}\right) \quad (4)$$

192 where  $es$  is the saturation vapor pressure [hPa],  $U$  is the relative humidity [%], and  $T_a$  [°C] is the  
 193 air temperature. The parameter  $es$  was calculated using the method of the World Meteorological  
 194 Organization (2008).

### 195 2.2.2 Lateral boundary condition

196 The average water temperature and salinity of each day of the year are calculated from  
 197 monthly observation data (observation point number A10, latitude 34.37325, longitude  
 198 137.21583, measurement depth: 0, 10, 20, 30, 50, 75, 100, and 150 m below sea level) for 10  
 199 years (2004 to 2013) obtained by the Aichi Fisheries Research Institute. Their data were used to  
 200 generate the lateral boundary conditions of water temperature and salinity. The observation data  
 201 were uniformly interpolated in the horizontal direction, linearly interpolated in the vertical  
 202 direction, and linearly interpolated in the time direction. The tide level for the lateral boundary  
 203 conditions was estimated using the amplitude and phase of 14 major tide components (Sa, Ssa,  
 204 Mm, MSf, Mf, Q1, O1, P1, S1, K1, N2, M2, S2, K2) obtained from observation data of the  
 205 Akabane tide station (latitude 34.6, longitude 137.18333) located near the lateral boundary. The  
 206 estimated tide level was corrected using the atmospheric pressure.

### 207 2.2.3 River discharge forcing

208 The river discharge was calculated by a storage function method, as follows.

$$\frac{ds}{dt} = q_{up}(t) + r(t) - q(t) - q_{base} \quad (5)$$

$$s = k_1 q^p + k_2 \frac{dq}{dt} \quad (6)$$

$$Q(t) = \frac{q(t)}{3.6} A \quad (7)$$

212 where  $s$  is the apparent storage height of the basin [mm],  $t$  is time [h],  $r$  is the average  
 213 precipitation in the basin [mm h<sup>-1</sup>],  $q$  is the runoff over time  $t$  [mm h<sup>-1</sup>],  $q_{up}$  is the runoff from the  
 214 upper area [mm h<sup>-1</sup>],  $q_{base}$  is the base runoff [mm h<sup>-1</sup>],  $k_1$ ,  $k_2$ , and  $p$  are constant values,  $Q$  is the

215 river discharge [ $\text{m}^3 \text{s}^{-1}$ ], and  $A$  is the basin area [ $\text{km}^2$ ]. Equation (6) is based on Prasad (1967).  
 216 For the class A river in the basin,  $k_1$ ,  $k_2$ , and  $p$  were obtained to compare the observed river  
 217 discharge values. For other smaller rivers, few river discharge observations are made during  
 218 precipitation events; therefore, the parameters were estimated using the average precipitation  
 219 value in the basin multiplied by the basin area to obtain the river discharge. The average  
 220 precipitation ( $r$ ) in each basin was calculated as follows. Each river basin was divided into a grid.  
 221 The distance between each grid point and the AMeDAS observation point was calculated, and  
 222 any AMeDAS data point less than 30 km from a grid point was extracted. Here, the maximum  
 223 number of AMeDAS observation points used at each grid point was 10. Precipitation at each grid  
 224 was calculated by weighting according to the same method used for other weather data. The sum  
 225 of precipitation for each grid was taken as the average precipitation of the basin.

226 River water temperature was calculated from the air temperature near the mouth of the  
 227 river using Eq. (8):

$$228 \quad T_w = aT_a + b \quad (8)$$

229 where  $T_w$  [ $^{\circ}\text{C}$ ] is the river water temperature, and  $a$  and  $b$  are parameters calculated from the  
 230 relationship between the observed air temperature near the river mouth and the observed river  
 231 water temperature.

### 232 2.3 Assimilation model

233 The EnKF model for the Ise Bay Simulator was coded (Matsuzaki & Inoue, 2020) based  
 234 on the work of Evensen (2003). The settings for the ensemble simulation were the same as those  
 235 described in section 2.1, and a novel data assimilation method with a high-resolution horizontal  
 236 grid size (800 m) was employed. EnKF was implemented with 32 members. The ensemble  
 237 number was chosen by referring to a previous study (Matsuzaki & Inoue, 2020). The observation  
 238 data described below were assimilated once per day at 00:00. No localization technique was  
 239 applied (Evensen, 2009; Gaspari & Cohn, 1999; Hamill et al., 2001); thus, it was possible to  
 240 correct the entire Ise Bay based on the background error covariance using a physical model,  
 241 instead of non-physical techniques such as the distance function. The multiplicative inflation  
 242 technique was not applied because multiplicative inflation generates artificial vertical  
 243 background error covariance (Sanikommu et al., 2020). Moreover, correlation of the observation  
 244 error was ignored, i.e., the observation error covariance matrix was set to diagonal. As explained  
 245 in section 2.4, perturbations were added to the boundary conditions to represent the system error.  
 246 When assimilation was performed near the lateral boundary, the assimilation system became  
 247 unstable. To stabilize the data assimilation, the two meshes adjacent to the lateral boundary were  
 248 excluded from the assimilation, which ensured stable data assimilation performance.

### 249 2.4 Method of adding perturbations to boundary conditions

250 Generating a perturbation and determining its magnitude is a challenging task. Previous  
 251 research has employed various methods to determine the boundary conditions for expressing an  
 252 ensemble containing system noise, e.g.: (i) a method of adding noise according to a normal  
 253 distribution (Turner et al., 2008), (ii) a method of adding red noise (Evensen, 2003; Sakov et al.,  
 254 2012), (iii) a method of using ensemble simulation results (Bougeault et al., 2010) as the  
 255 boundary condition (Sanikommu et al., 2020), and (iv) a method that considers the difference in  
 256 state quantities at different times as a perturbation (Kunii & Miyoshi, 2012). This study  
 257 employed method (i), as shown in Equation (9), because it was previously used to conduct

258 successful data assimilation for a coastal estuary; however, the study of Turner et al. (2008)  
 259 employed OSSE instead of real data.

$$260 \quad \mathbf{F}_{mem} = \mathbf{F}_{base} + \mathbf{v} \quad (9)$$

261 Here,  $\mathbf{F}_{mem}$  indicates the boundary conditions for data assimilation with perturbation,  $\mathbf{F}_{base}$   
 262 indicates the boundary conditions for numerical simulation, and  $\mathbf{v}$  indicates the perturbations that  
 263 have a normal distribution with a mean of zero and variance of  $\zeta^2$ . For some boundary  
 264 conditions, such as that shown in Equation (9), the additive method is not valid. For example, the  
 265 boundary condition of river discharge may have a negative value when the river discharge is  
 266 close to zero and noise with a normal distribution is added. In addition, when river discharge is  
 267 larger, the error of river discharge forcing appears to increase. Thus, the following multiplication  
 268 method was introduced:

$$269 \quad \mathbf{F}_{mem} = \mathbf{v}\mathbf{F}_{base} \quad (10)$$

270 The model outputs evaluated in this study, which are explained in section 2.7, are water  
 271 temperature and salinity. The boundary conditions considered having a large effect on the  
 272 simulation error of water temperature and salinity were selected as follows. For the numerical  
 273 simulation model, the atmospheric forcing boundary conditions include air temperature,  
 274 shortwave radiation, longwave radiation, atmospheric pressure, wind direction, wind speed,  
 275 water vapor pressure, and precipitation. The lateral boundary conditions include water  
 276 temperature, salinity, and water level. The river discharge forcing boundary conditions include  
 277 river discharge and river water temperature. Of these, the errors in the boundary conditions of air  
 278 temperature, shortwave radiation, longwave radiation, lateral boundary water temperature, and  
 279 river water temperature were considered directly linked to the numerical simulation error of  
 280 water temperature. Similarly, the errors in the boundary conditions of precipitation, lateral  
 281 boundary salinity, and river discharge were considered directly linked to the numerical  
 282 simulation error of salinity. In addition, as water temperature and salinity are advected and  
 283 diffused by the flow of water mass, the errors in the boundary conditions of wind speed,  
 284 atmospheric pressure, and tide level of the lateral boundary were also considered having an  
 285 effect. For these boundary conditions, these three assumptions were set. First, the shortwave  
 286 radiation and longwave radiation errors were included in the air temperature error. Second, the  
 287 precipitation error was included in the river discharge error. Third, the influence of the error  
 288 between the atmospheric pressure and the tide level of the lateral boundary was relatively small,  
 289 so was ignored. Therefore, the perturbations for atmospheric forcing were air temperature and  
 290 wind speed, the perturbations for lateral boundary conditions were water temperature and  
 291 salinity, and the perturbations for river discharge forcing were river discharge and river water  
 292 temperature.

293 As the magnitude of the error is considered to correlate with the accuracy of the boundary  
 294 conditions, the magnitude of the perturbation,  $\zeta$ , for creating the ensemble must be determined  
 295 by the same method used to generate the boundary conditions. In this study,  $\zeta$  values were  
 296 estimated according to the assumption that all calculated error distributions follow a normal  
 297 distribution;  $\zeta$  values calculated on a trial basis are shown in *Appendix A* and summarized in  
 298 **Table 1**. When the normal distribution is expressed by a normal random number with a few  
 299 members, there is the potential for a large deviation from the normal distribution due to sampling  
 300 error. In this study, we did not use normal random numbers, but set the value of each member to

301 match the cumulative value of the normal distribution so the normal distribution can be  
 302 expressed even with a few members. To avoid unintended correlation of each boundary  
 303 condition, the Fisher-Yates shuffle (Fisher & Yates, 1948) was used to perform 10,000  
 304 replacement attempts, and the boundary conditions were set for each ensemble member using the  
 305 combination with the lowest correlation.

306

307 **Table 1.** Magnitude of perturbations to boundary conditions. Calculation of  $\xi$  values is shown in  
 308 Appendix A.

Boundary condition		Method	$\xi$
Atmospheric forcing	Air temperature	Equation (9)	3.04 °C
	Wind speed	Equation (9)	3.45 m s <sup>-1</sup>
Lateral boundary conditions	Water temperature	Equation (9)	0.73 °C
	Salinity	Equation (9)	0.20
River discharge forcing	River discharge	Equation (10)	0.35
	River water temperature	Equation (9)	1.21 °C

309 2.5 Assimilated observations

310 In situ water temperature and salinity profiles observed at fixed points were used for the  
 311 data assimilation. Seven in situ observation stations are in operation in Ise Bay. Data from the  
 312 five observation stations in **Table 2** were assimilated. Observation error variance values were set  
 313 to (1.0 °C)<sup>2</sup> for water temperature and (1.0)<sup>2</sup> for salinity. These values were set referring to a  
 314 previous study (Matsuzaki & Inoue, 2020). Gross error check was performed as background  
 315 quality control. The difference between the observed value and the first guess value was  
 316 calculated, and if the difference was over 3 °C for water temperature, and 6 for salinity; the  
 317 observed value was rejected.

318

319 **Table 2.** Assimilated observation data.

No.	Station name	Latitude (°N)	Longitude (°E)	Observation type	Observation depth [m]
A1	Back of Ise Bay	34.926	136.741	Automatic elevating	Every 1.0 m
A2	Center of Ise Bay	34.669	136.841	Automatic elevating	Every 1.0 m
A3	Mouth of Ise Bay	34.509	137.018	Fixed	1.0 m, 11.8 m, and 23.2 m from low water level
A4	No. 1 buoy	34.743	137.220	Automatic elevating	Every 1.0 m
A5	No. 2 buoy	34.745	137.072	Automatic elevating	Every 1.0 m

## 320 2.6 Experimental setup

321 Experiments were conducted for six cases (**Table 3**). In the standard experiment (case 1),  
 322 data assimilation was not applied, i.e., case 1 was a normal numerical simulation. Case 2  
 323 included the optimal settings determined before the experiment. Perturbations were applied to  
 324 three boundary conditions: atmospheric forcing, lateral boundary conditions, and river discharge  
 325 forcing. Cases 3–6 included the assimilation results but used different methods of generating the  
 326 ensembles. These experiments were conducted to confirm the effect of adding perturbations to  
 327 the boundary conditions by comparing the results with those of case 2. Case 3 had the same  
 328 conditions as case 2 but did not perturb the atmospheric forcing of air temperature and wind  
 329 speed, it analyzed the effect of considering the uncertainty of atmospheric forcing on the data  
 330 assimilation results. As case 4 applied perturbations to air temperature but not to wind speed, it  
 331 isolated the effects of air temperature and wind speed among the atmospheric forcing boundary  
 332 conditions. Finally, as cases 5 and 6 had the same conditions as case 2 but did not perturb the  
 333 lateral boundary conditions (case 5) or river discharge forcing (case 6), these experiments  
 334 examined the effect of considering the uncertainty of lateral boundary conditions and river  
 335 discharge forcing on the data assimilation results. The assimilation experiments were conducted  
 336 for one year from 1 January 2016, to evaluate the applicability of the proposed method to long-  
 337 term fluctuations, including seasonal changes, and to verify the robustness of the data  
 338 assimilation method. Initial ensembles for the assimilation experiments on 1 January 2016 were  
 339 generated using an eight-month spin-up period from 1 April 2015. Still, in the spin-up period, the  
 340 ensemble members were calculated under the boundary conditions including the perturbations,  
 341 and exhibited an ensemble spread according to the position and magnitude of the perturbation of  
 342 the initial conditions.

343 **Table 3.** Experimental conditions.

Experiment	Assimilation	Atmospheric forcing		Lateral boundary condition	River discharge forcing
		Air temperature	Wind speed		
Case 1	Control run without DA	NA	NA	NA	NA
Case 2	Assimilated	Perturbed	Perturbed	Perturbed	Perturbed
Case 3	Assimilated	Not perturbed	Not perturbed	Perturbed	Perturbed
Case 4	Assimilated	Perturbed	Not perturbed	Perturbed	Perturbed
Case 5	Assimilated	Perturbed	Perturbed	Not perturbed	Perturbed
Case 6	Assimilated	Perturbed	Perturbed	Perturbed	Not perturbed

## 344 2.7 Accuracy validation

345 Water temperature and salinity data of the model output were compared with the in situ  
 346 observation data of water temperature and salinity profiles observed at fixed points (**Table 4**). As  
 347 it was impossible to prepare observation values such as SST for salinity, the model outputs and  
 348 data used for the assimilation (**Table 2**) were compared to evaluate and discuss the effects of  
 349 perturbing boundary conditions to generate ensembles. Observation data were collected every  
 350 hour, but the assimilations were conducted every day; thus, comparisons were conducted every  
 351 day. Water temperature data of the model output were also compared with the SST data observed  
 352 by Terra and Aqua (Moderate Resolution Imaging Spectroradiometer: MODIS) to evaluate the  
 353 correction of water temperature in the spatial direction. The MODIS SST data were obtained by  
 354 assuming that all data observed between 22:00 and 02:00 were observed at midnight; the SST

355 data were then compared with model output data for assimilation. The reproducibility of the  
 356 planar distribution of water temperature was then discussed.

357 **Table 4.** Comparison observation data not assimilated.

No.	Station name	Latitude (°N)	Longitude (°E)	Observation type	Observation depth
C1	Nakayama Channel	34.623	136.982	Fixed	1.4 m, 8.2 m, 12.4 m from low water level
C2	No. 3 buoy	34.675	137.097	Automatic elevating	Every 1.0 m

358

359 The accuracy of the model output was evaluated using two indices: the bias (Equation 10)  
 360 and the root-mean-square error (RMSE, Equation 11):

$$361 \quad bias = \frac{1}{N} \sum_{i=1}^N e_i \quad (10)$$

$$362 \quad RMSE = \sqrt{\frac{1}{N} \sum_{i=1}^N e_i^2} \quad (11)$$

363 where  $e_i$  is the simulation error (model output minus observation) and  $N$  is the number of model  
 364 outputs and observations. As degeneration of the ensemble spread becomes a problem when  
 365 executing EnKF (termed as filter divergence), the magnitude of the ensemble spread was  
 366 evaluated (Equation 12):

$$367 \quad Ensemble\ spread = \sqrt{\frac{1}{mem-1} \sum_{i=1}^{mem} (x_i - \bar{x})^2} \quad (12)$$

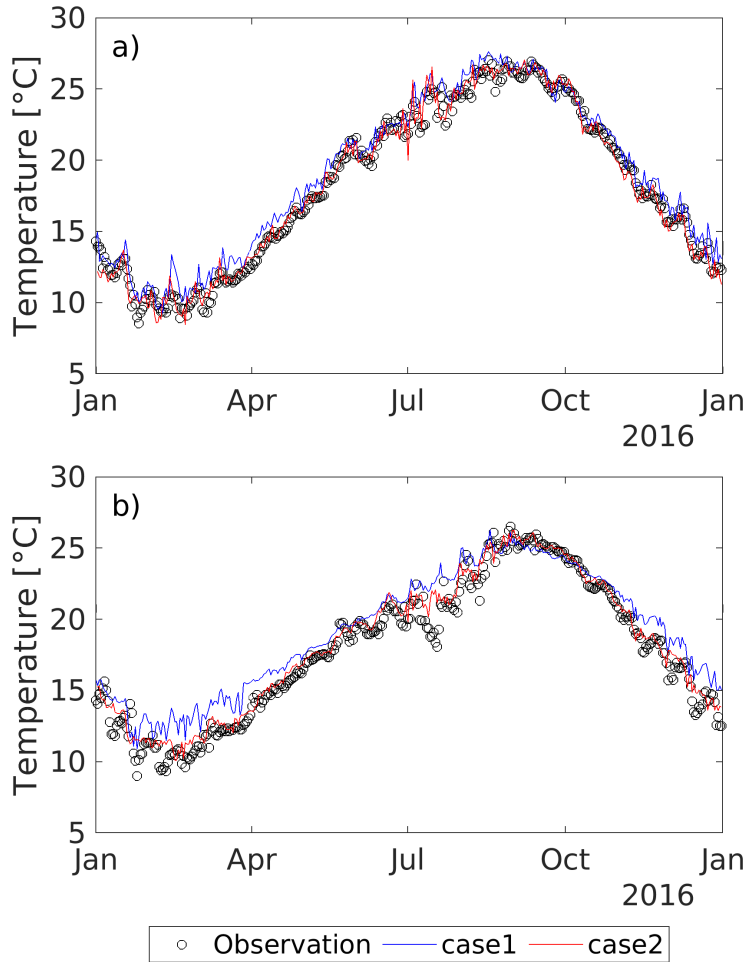
368 where  $mem$  is the number of ensemble members ( $mem$  equals 32),  $x$  is a variable, and  $\bar{x}$  is the  
 369 average value of  $x$ .

### 370 **3 Results**

#### 371 **3.1 Performance and robustness of data assimilation**

372 In this section, the results of the control run (case 1) and data assimilation (case 2) are  
 373 compared to show the validity and effectiveness of the data assimilation method. Figure 2 and  
 374 Figure 3 compare the time series of observed water temperature data in Nakayama Channel and  
 375 at the No. 3 buoy (Table 4) and the model output of case 1 and case 2. Case 1 exhibits the same  
 376 water temperature fluctuation trend as the observed values; however, the water temperature is  
 377 higher than the observed values. This difference is particularly large in the lower layer. Case 2  
 378 shows the water temperature corrected to match the observations. Moreover, case 2 was possible  
 379 to carry out the data assimilation for one year without breaking the calculation. Figure 4 and  
 380 Figure 5 show the biases and RMSEs between the observed and simulated water temperatures for  
 381 Nakayama Channel and the No. 3 buoy. Bias and RMSE values are lower for case 2 than case 1  
 382 at all depths. The bias improvement is approximately the same near the water surface and near  
 383 the bottom, with an average difference between case 1 and case 2 of 0.78 °C for Nakayama  
 384 Channel and 1.09 °C for the No.3 buoy. Conversely, the RMSE improvement is greater near the

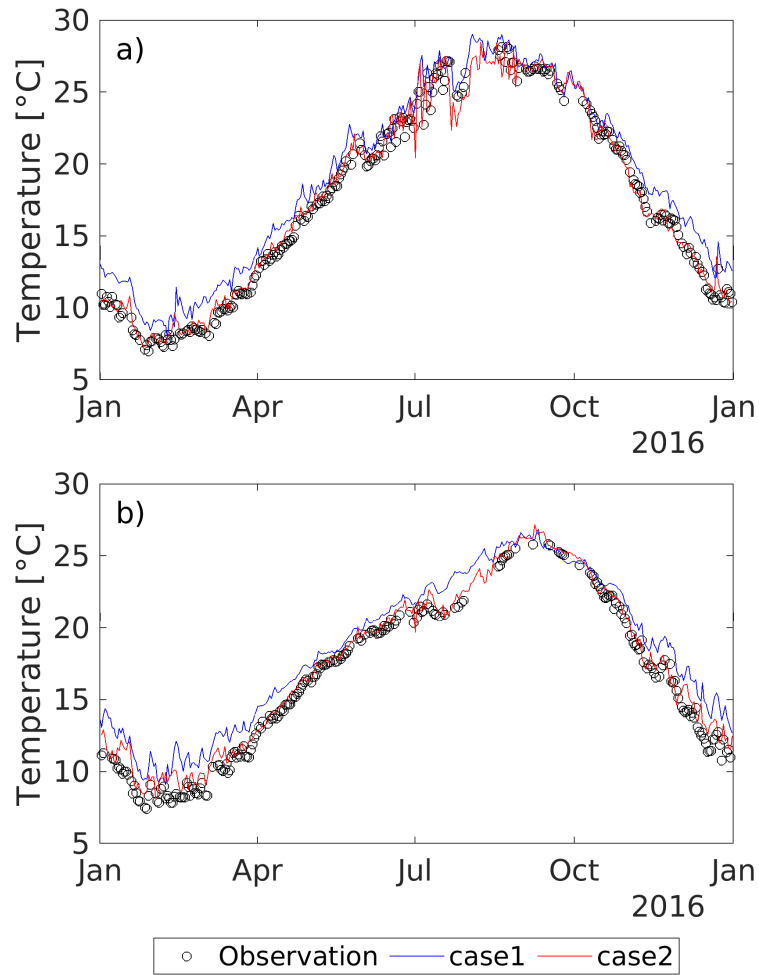
385 bottom than near the sea surface. The average difference between case 1 and case 2 is 0.57 °C for  
 386 Nakayama Channel and 0.86 °C for the No.3 buoy. These results indicate that the proposed  
 387 regional data assimilation method for a coastal estuary is effective for correcting water  
 388 temperature and highly robust, i.e., it can be applied throughout the year and reflects seasonal  
 389 variations.



390

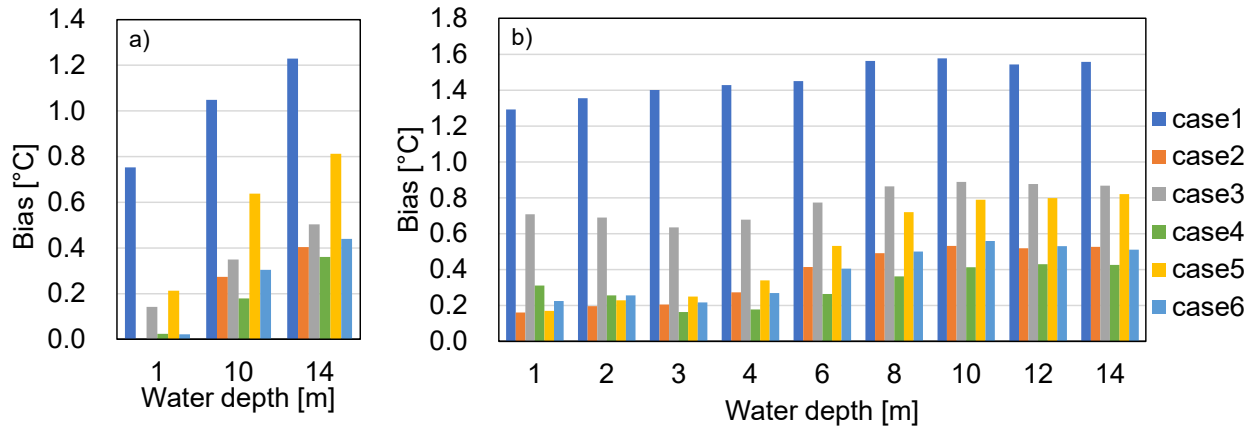
391 **Figure 2.** Timeseries of water temperature data at Nakayama Channel for observations, case 1,  
 392 and case 2. a) water depth of 1.0 m; b) water depth of 12.0 m.

393



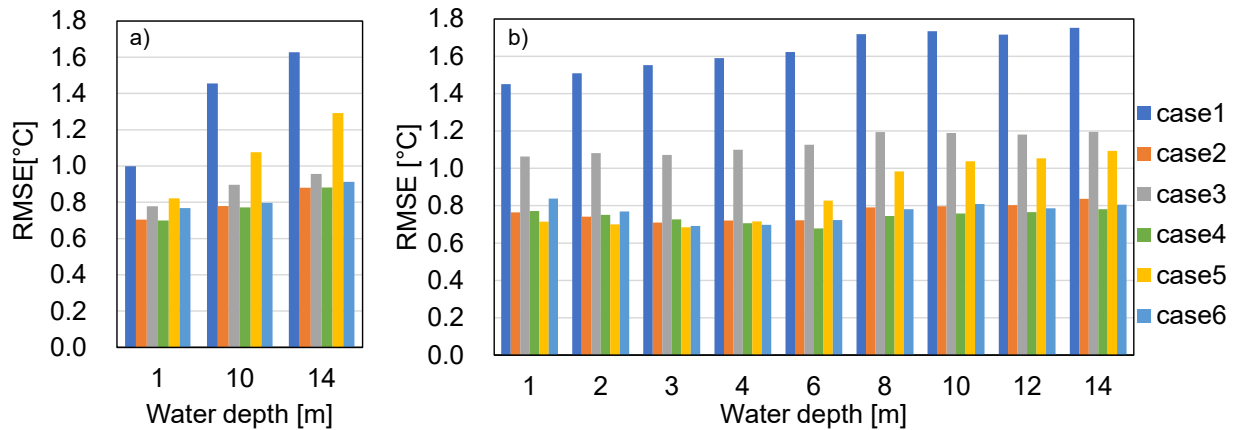
394

395 **Figure 3.** Timeseries of water temperature data at the No.3 buoy for observations, case 1, and  
396 case 2. a) water depth of 1.0 m; b) water depth of 12.0 m.  
397



398  
399 **Figure 4.** Bias between observed and modeled water temperature for all experiments. a)  
400 Nakayama Channel; b) No.3 buoy.

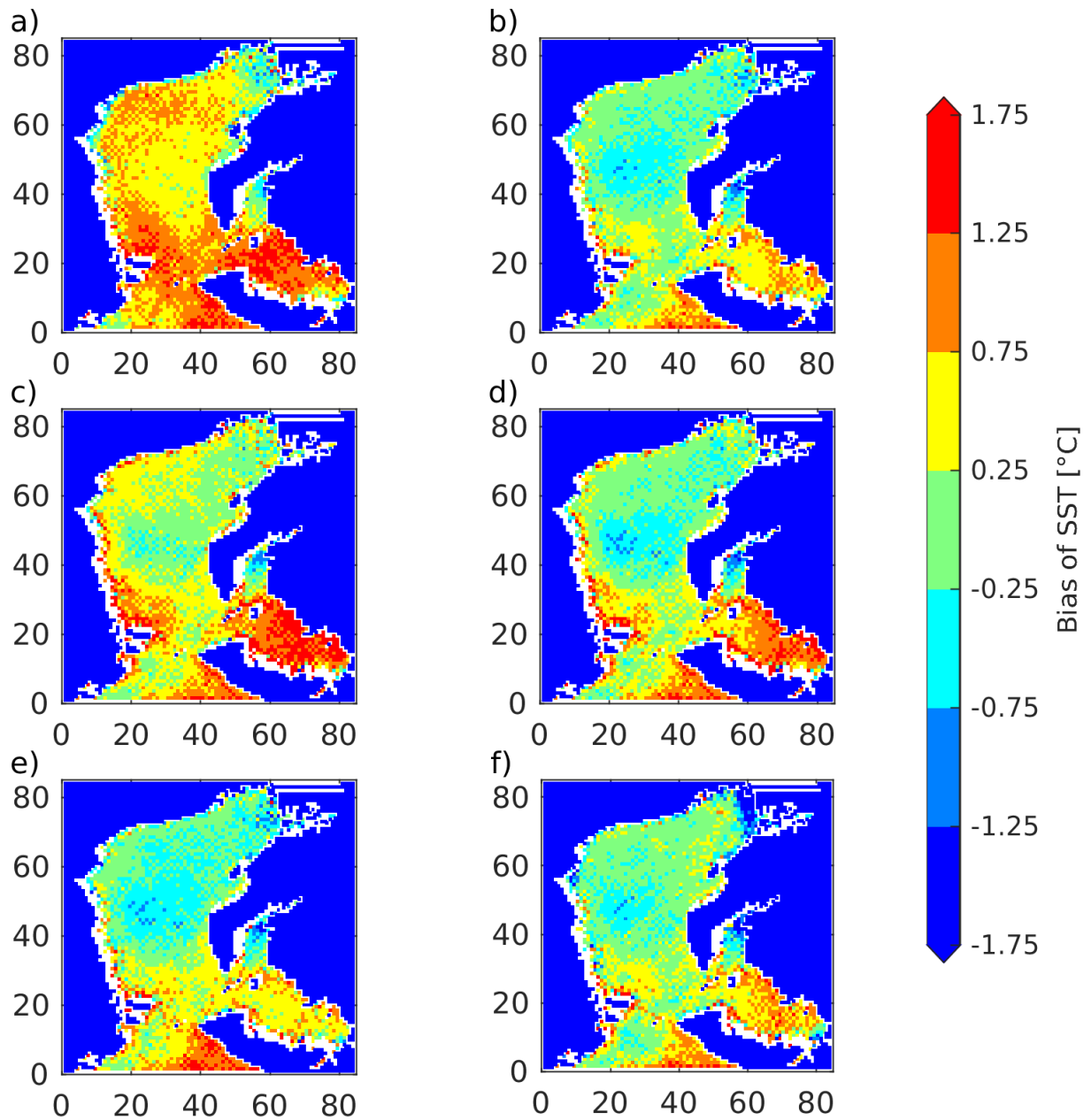
401



402  
403 **Figure 5.** RMSE between observed and modeled water temperature for all experiments. a)  
404 Nakayama Channel; b) No.3 buoy.

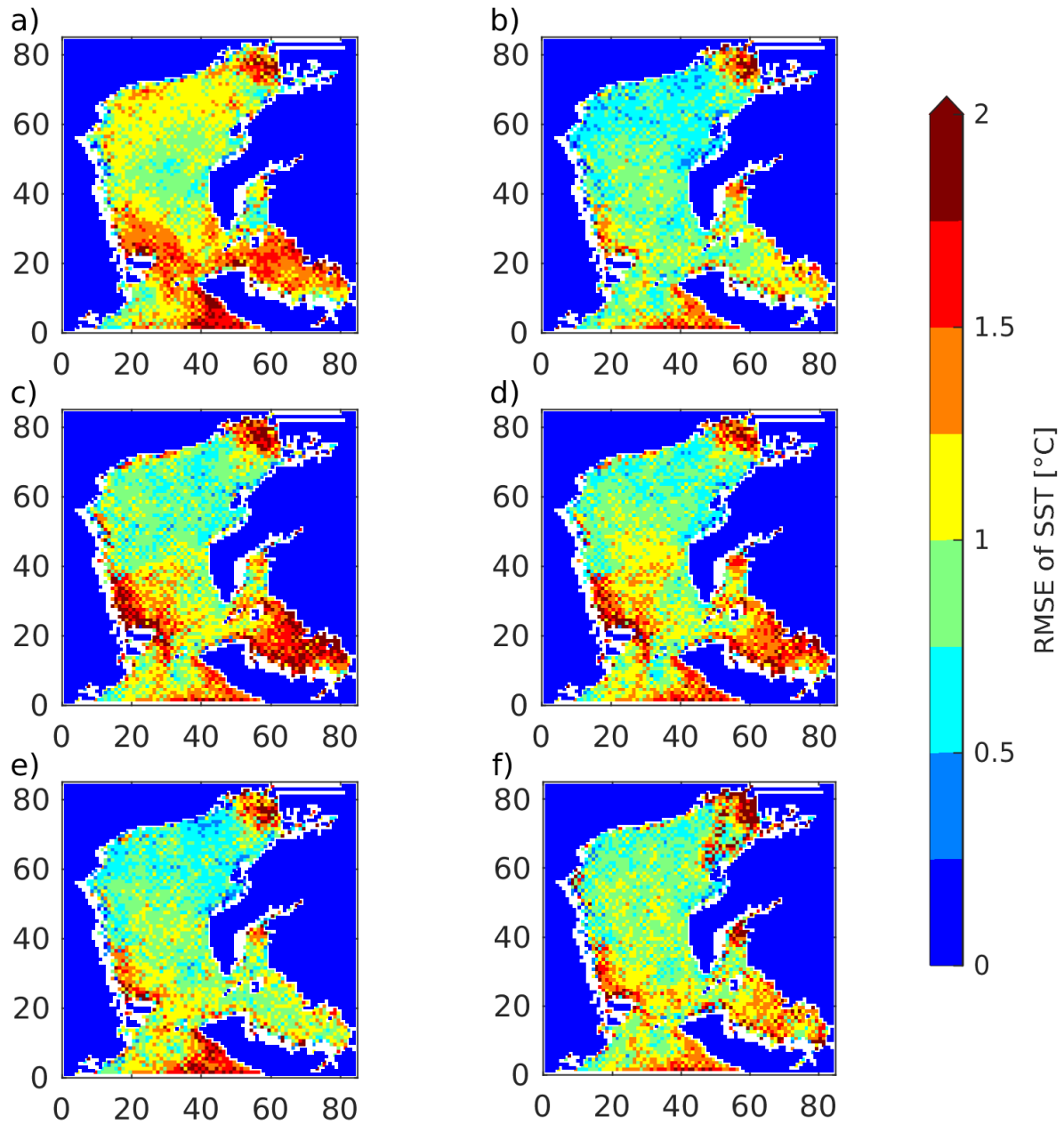
405

406 Figure 6 and Figure 7 show the spatial distributions of bias and RMSE values between  
407 SST data observed by MODIS and the model outputs. The bias and RMSE values of case 2 data  
408 are lower than those of case 1 throughout Ise Bay, particularly at the west side of the bay,  
409 although the observed values used for data assimilation extend from the center of the bay to the  
410 east side, and there are no observation points on the west side. Data assimilation corrects the  
411 water temperature for the entire bay, despite sparse observations in the horizontal direction,  
412 because the error covariance is properly expressed by the proposed perturbation. Moreover, the  
413 bias and RMSE values of SST are 0.67 °C and 0.52 °C lower, respectively, in case 2 (Figure 8).  
414 Nevertheless, the bias and RMSE values do not exhibit substantial improvement on the east side  
415 of the bay mouth and in parts of the back of the bay. Thus, there is still room for further  
416 improvement.



417

418 **Figure 6.** Planar images of the SST bias for a) case 1, b) case 2, c) case 3, d) case 4, e) case 5,  
419 and (f) case 6. The horizontal and vertical axes indicate a calculation grid of  $85 \times 85$ .  
420

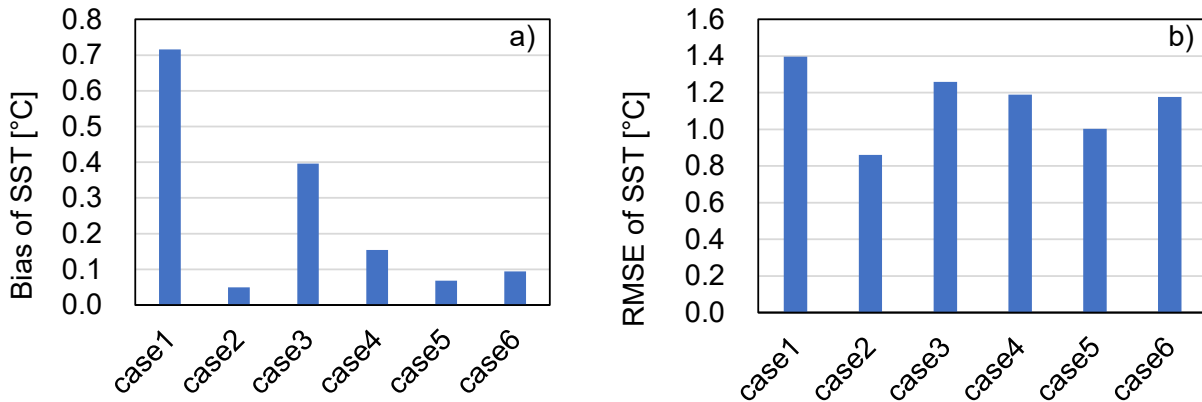


421

422 **Figure 7.** Planar images of the RMSE values of SST for a) case 1, b) case 2, c) case 3, d) case 4,  
423 e) case 5, and (f) case 6. The horizontal and vertical axes indicate a calculation grid of 85 × 85.

424

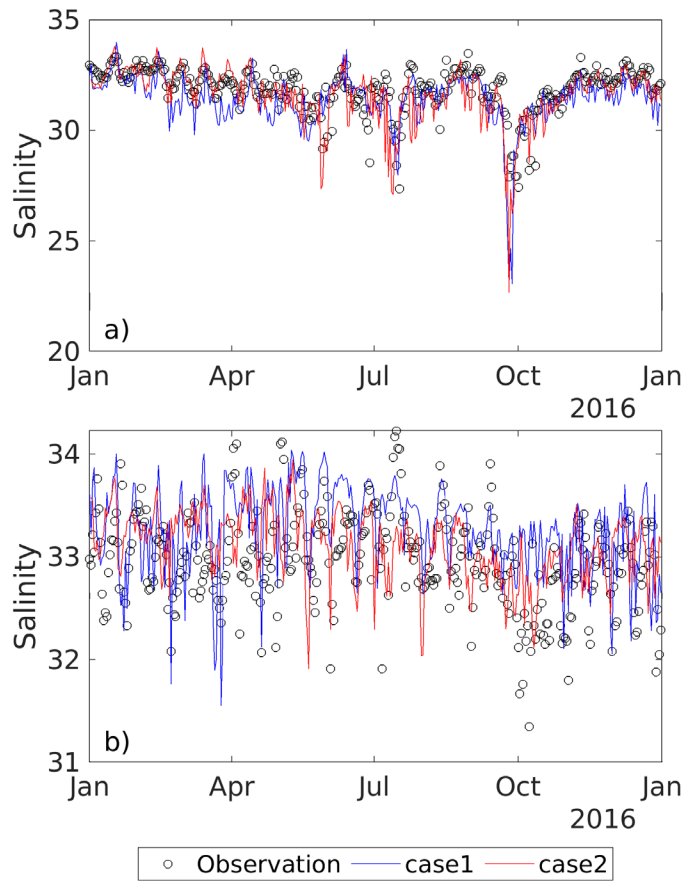
425



426

427 **Figure 8.** a) Bias and b) RMSE values of SST for all experiments.

428 Figure 9 and Figure 10 show time series of the observed salinity in Nakayama Channel  
 429 and at the No. 3 buoy and the model outputs of case 1 and case 2. Although the effect of  
 430 assimilation on salinity is not as clear as that for water temperature, the assimilation performance  
 431 is stable throughout the year. Figure 11 and Figure 12 show the bias and RMSE values of salinity  
 432 in Nakayama Channel and at the No. 3 buoy. Bias and RMSE values decrease from case 1 to  
 433 case 2 at all depths in Nakayama Channel. The average difference in bias and RMSE values  
 434 between the two experiments are 0.17 and 0.06, respectively. At the No. 3 buoy, the bias values  
 435 are lower at all depths in case 2; however, the RMSE values do not show this trend; the average  
 436 difference in bias and RMSE values between the two experiments are 0.07 and -0.09,  
 437 respectively. One reason for this finding could be that the magnitude of perturbations ( $\xi$ ) for  
 438 assimilation of salinity data was not appropriate in the boundary conditions. When data  
 439 assimilation is performed by only changing the magnitude of the perturbation of the boundary  
 440 conditions from case 2 (the results of the sensitivity experiments are not shown, but  $\xi$  was set to  
 441 1.00 °C for air temperature, 2.00 m s<sup>-1</sup> for wind speed, 0.50 °C and 0.25 for water temperature  
 442 and salinity of the lateral boundary, 0.36 for river discharge, and 0.50 °C for river water  
 443 temperature), the average RMSE of salinity at the No. 3 buoy is 0.01 smaller for case 2 than case  
 444 1. Therefore, the optimal magnitude of perturbation should be carefully considered.  
 445 Nevertheless, the results indicate that the proposed regional data assimilation method for coastal  
 446 estuaries is an effective and robust method for both water temperature and salinity data.

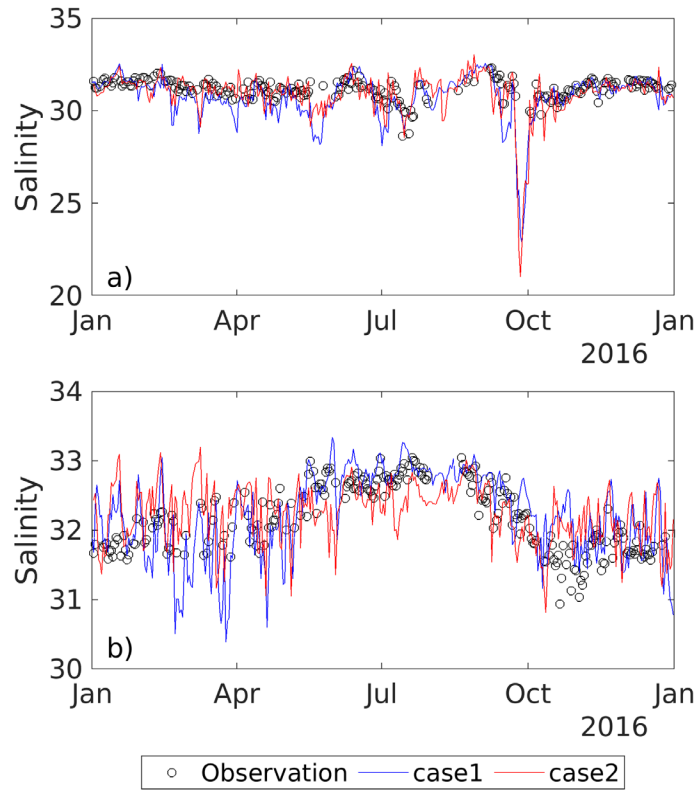


447

448 **Figure 9.** Timeseries of salinity at Nakayama Channel for observations, case 1, and case 2. a)  
449 water depth at 1.0 m; b) water depth at 12.0 m.

450

451

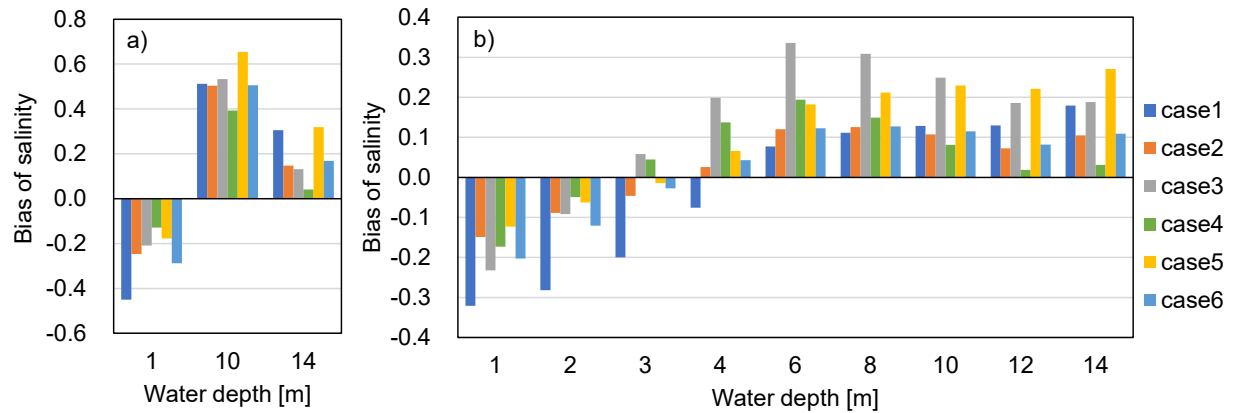


452

453 **Figure 10.** Timeseries of salinity at the No.3 buoy for observations, case 1, and case 2. a) water  
454 depth at 1.0 m; b) water depth at 12.0 m.

455

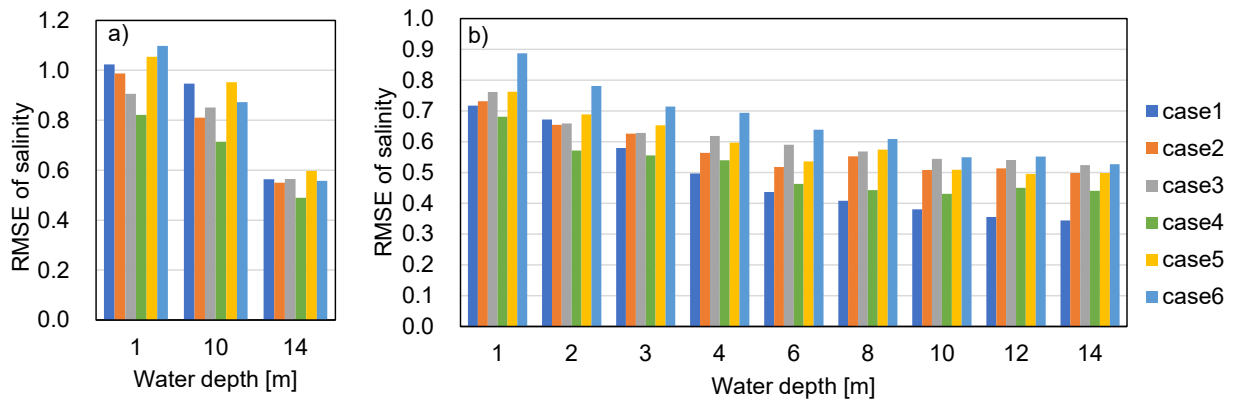
456



457

458 **Figure 11.** Bias between observed and modeled salinity for all experiments. a) Nakayama  
459 Channel; b) No.3 buoy.

460



461

462 **Figure 12.** RMSE between observed and modeled salinity for all experiments. a) Nakayama  
463 Channel; b) No.3 buoy.

464

### 3.2 Effect of perturbations on boundary conditions

465

#### 3.2.1 Atmospheric forcing

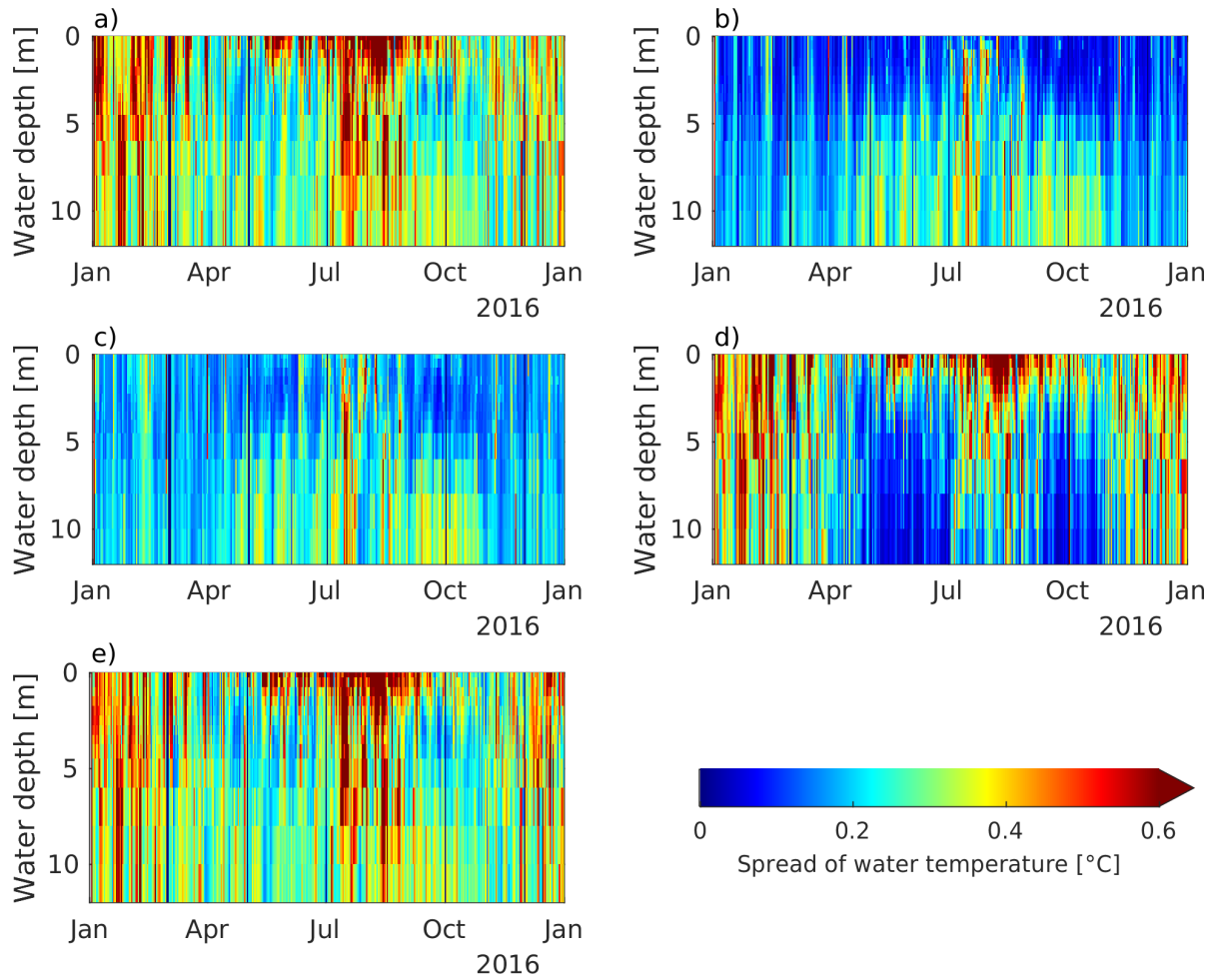
466

467 This subsection examines the effect of perturbation on atmospheric forcing on the data  
468 assimilation results. Compared to case 2, case 3, which does not perturb the air temperature and  
469 wind speed, does not improve the bias and RMSE values of water temperature in Nakayama  
470 Channel and at the No. 3 buoy (Figure 4 and Figure 5). This finding is particularly remarkable at  
471 the No. 3 buoy. Case 3 is the least improved among the data assimilation results (cases 2–6) for  
472 the bias and RMSE scores of both water temperature and SST (Figure 8). However, case 4,  
473 which perturbs the atmospheric forcing condition of air temperature, improves the water  
474 temperature from that of case 3 (Figure 4, Figure 5, and Figure 8). Case 4 also exhibits better  
475 bias and RMSE scores than case 2 at a depth of  $-4$  m or more at the No. 3 buoy, and better bias  
476 scores at a depth of  $-10$  m or more in the Nakayama Channel. On the other hand, case 4 does not  
exhibit improvements from case 2 at the other depths, in the SST in Mikawa Bay on the east side

477 of Ise Bay (Figure 6 and Figure 7), or in the SST bias and RMSE scores (**Figure 8**). Therefore,  
478 the scores of case 2 are generally better than those of case 4. The ensemble spread of water  
479 temperature in the Nakayama Channel (Figure 13) is smaller in case 3 than in case 2, especially  
480 in the surface layer. Moreover, the ensemble spread of case 4 is larger than of case 3, but smaller  
481 than of case 2. At the No. 3 buoy (Figure 14), the ensemble spread of case 3 is even smaller than  
482 in the Nakayama Channel; thus, it is considered that the perturbation of air temperature and wind  
483 speed is a large error factor. Thus, perturbation of the atmospheric boundary conditions increases  
484 the ensemble spread of water temperature, especially near the surface layer, enabling effective  
485 assimilation of observed water temperature values.

486 For salinity (Figure 11 and Figure **12**), cases 3 and 4 exhibit similar bias and RMSE  
487 scores to case 2. However, at the No. 3 buoy (at a water depth of  $-4$  m or more in Figure 11) and  
488 in the center of the bay (at a water depth of  $-10$  m or less in Figure 15), the bias score is  
489 significantly worse. Therefore, it is considered preferable to perturb atmospheric forcing to avoid  
490 local salinity errors in the data assimilation. The difference in the ensemble spread of salinity is  
491 small between case 3 and case 4 (Figure 17 and Figure 18). In addition, the ensemble spread of  
492 cases 3 and 4 is smaller than of cases 5 and 6 (Figure 17 and Figure 18), particularly at the No. 3  
493 buoy. These results indicate that, among the boundary conditions, wind speed has the greatest  
494 influence on the magnitude of the salinity ensemble spread and can be dominant depending on  
495 the location.

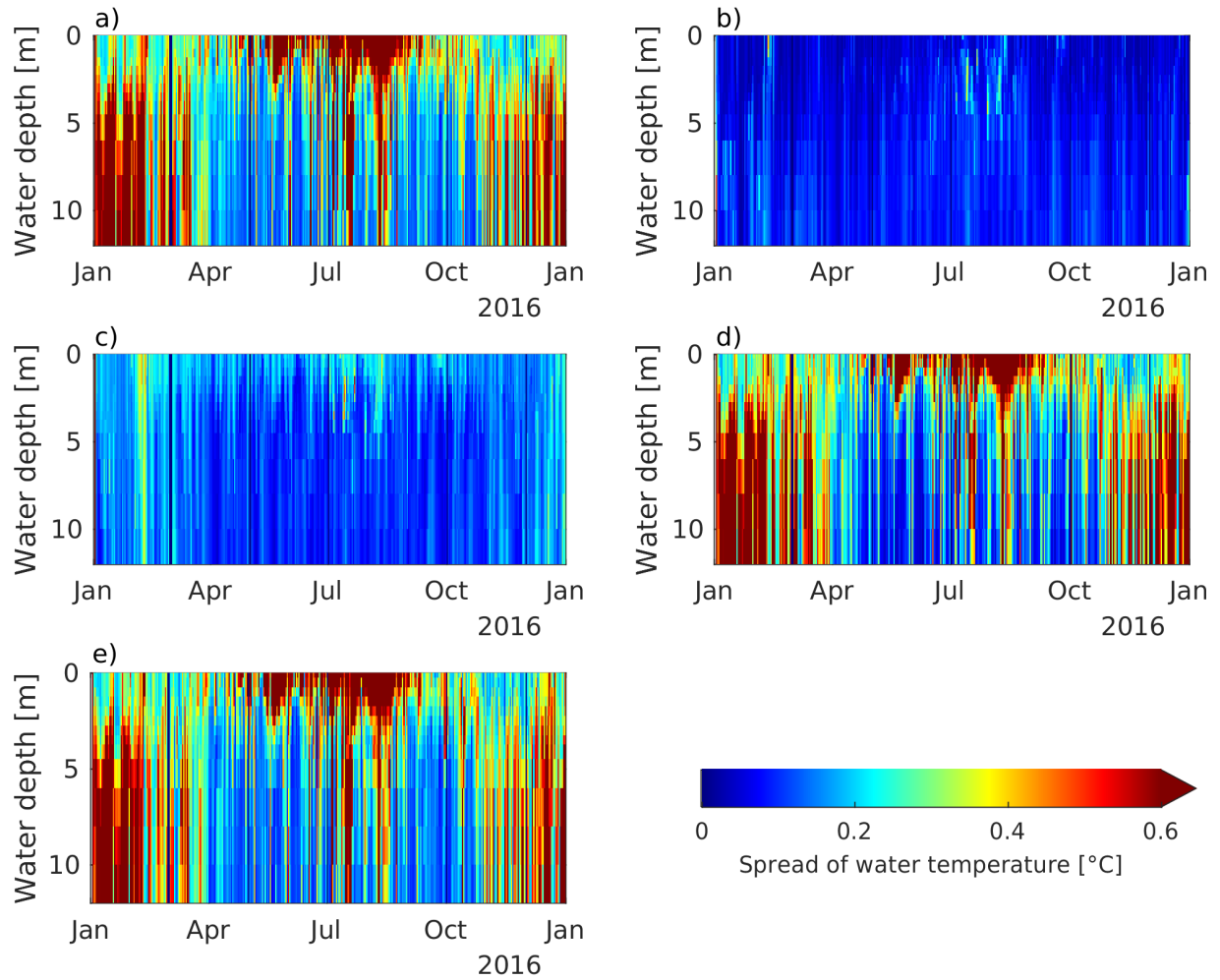
496



497

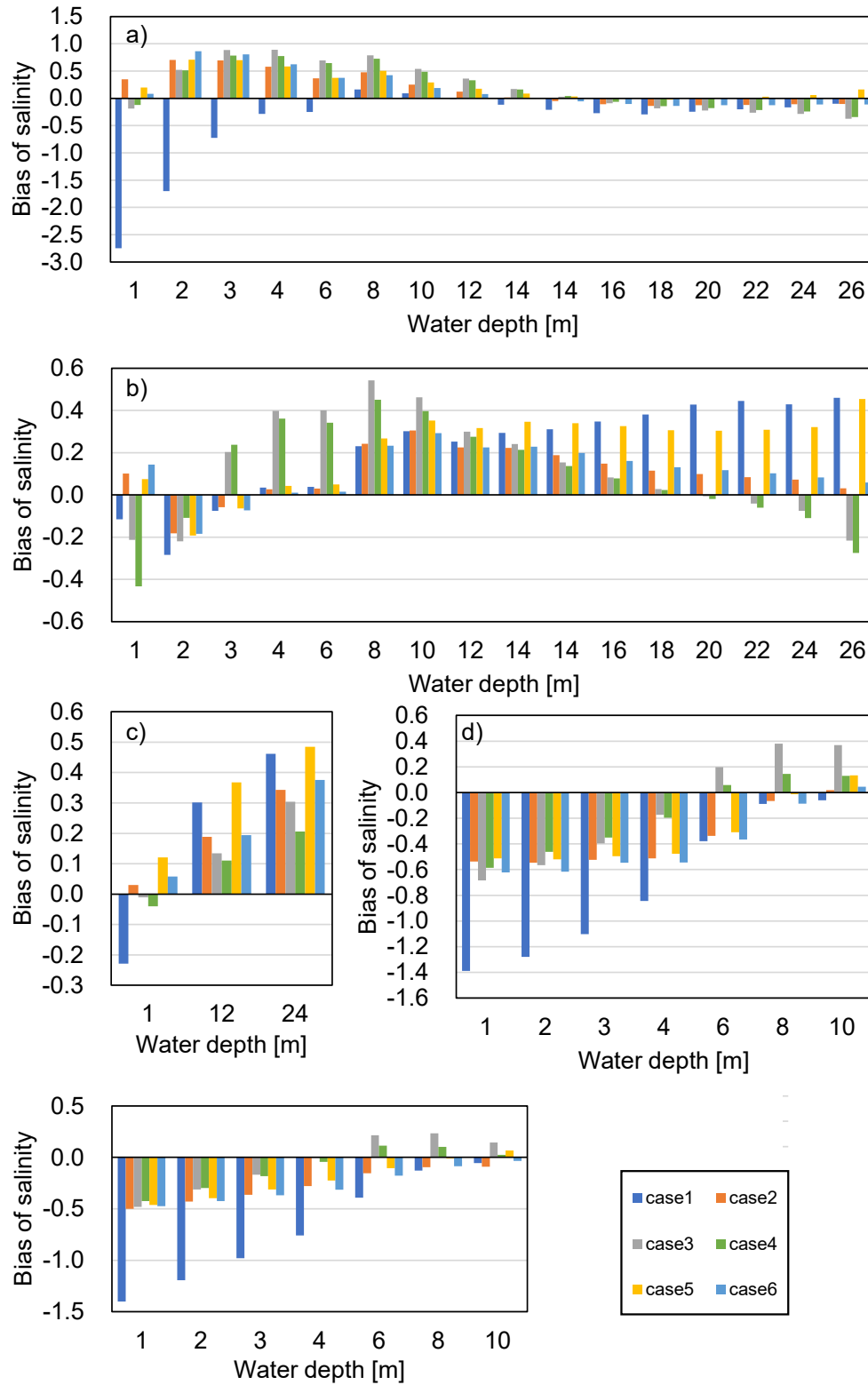
498 **Figure 13.** Temporal evolution of the ensemble spread of water temperature at Nakayama  
 499 Channel with water depth. a) Case 2, b) case 3, c) case 4, d) case 5, and e) case 6.

500



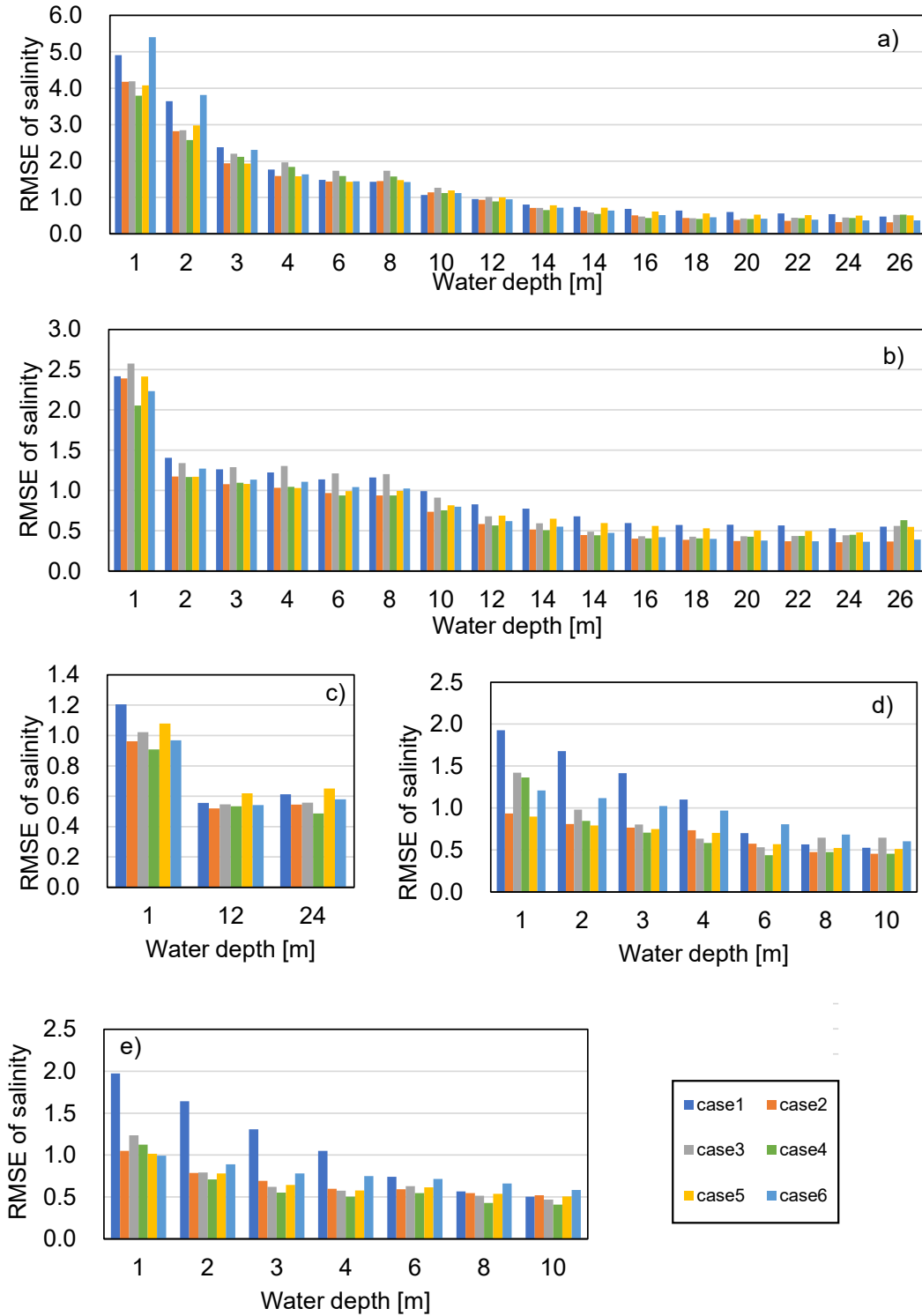
501

502 **Figure 14.** Temporal evolution of the ensemble spread of water temperature at the No. 3 buoy  
 503 with water depth. a) Case 2, b) case 3, c) case 4, d) case 5, and e) case 6.



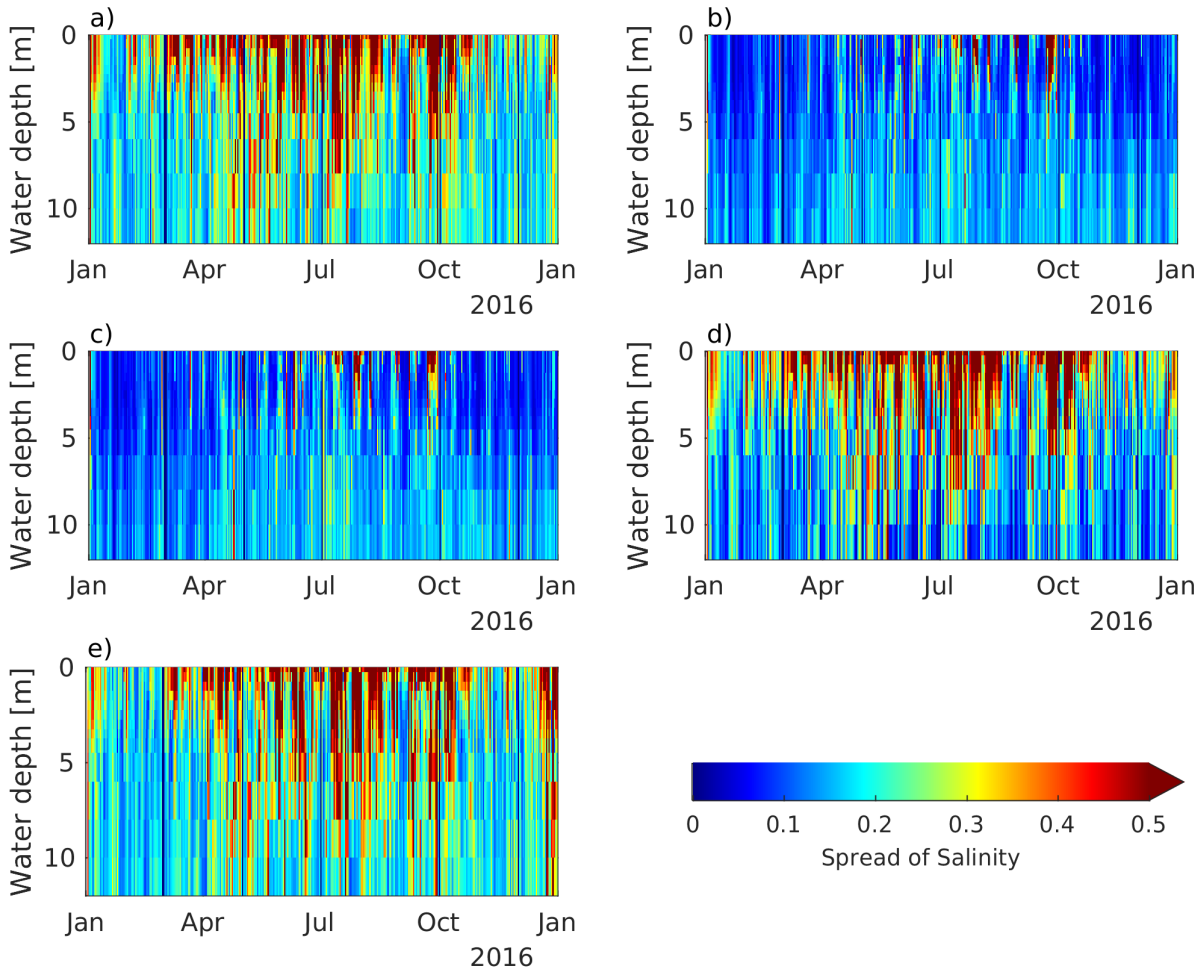
504

505 **Figure 15.** Bias of salinity between observations and model output using assimilated data from  
 506 Table 2. a) Back of bay, b) center of bay, c) mouth of bay, d) No. 1 buoy, and e) No. 2 buoy.



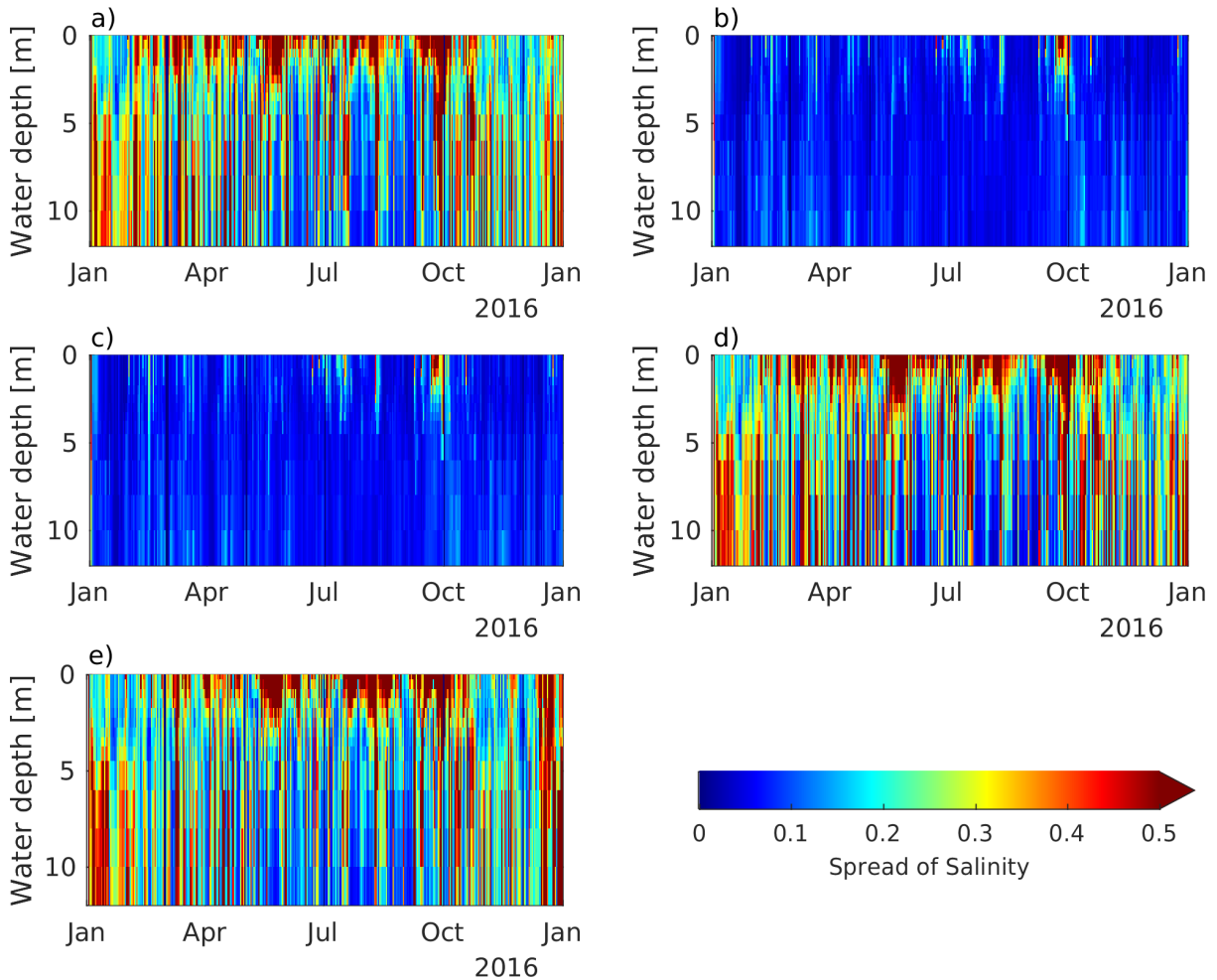
507

508 **Figure 16.** RMSE of salinity between observations and model output using assimilated data from  
 509 Table 2. a) Back of bay, b) center of bay, c) mouth of bay, d) No. 1 buoy, and e) No. 2 buoy.



510

511 **Figure 17.** Temporal evolution of the ensemble spread of salinity at Nakayama Channel with  
 512 water depth. a) Case 2, b) case 3, c) case 4, d) case 5, and e) case 6.



513

514 **Figure 18.** Temporal evolution of the ensemble spread of water temperature at the No. 3 buoy  
 515 with water depth. a) Case 2, b) case 3, c) case 4, d) case 5, and e) case 6.

516

### 517 3.2.2 Lateral boundary conditions

518 This section examines the effect of perturbation to the lateral boundary conditions on the  
 519 data assimilation results. In case 5, which does not perturb the lateral boundary conditions, the  
 520 bias and RMSE scores of water temperature in Nakayama Channel and at the No. 3 buoy are not  
 521 improved by data assimilation compared to those of case 2 (Figure 4 and Figure 5). This finding  
 522 is particularly remarkable in the Nakayama Channel. Case 5 exhibits the least improvement in  
 523 bias and RMSE scores among all data assimilation results (cases 2–6) in the Nakayama Channel  
 524 and no improvement in SST scores around the bay mouth (Figure 6 and Figure 7). The ensemble  
 525 spread of salinity is smaller for case 5 than for case 2 for all water depths in the Nakayama  
 526 Channel (Figure 13). The large ensemble spread for case 5 from January to March and in  
 527 December is thought to be because of perturbing the atmospheric boundary conditions because  
 528 the ensemble spread for case 3 during the same period is small. However, at the No. 3 buoy,  
 529 there is minimal difference in the ensemble spread between case 2 and case 5 (Figure 14).

530 Therefore, perturbation of the lateral boundary conditions increases the ensemble spread of water  
531 temperature at all water depths, especially near the bay mouth, and enables the effective  
532 assimilation of observed values.

533 Case 5 exhibits lower bias and RMSE scores for salinity than case 2 in the Nakayama  
534 Channel (Figure 11 and Figure 12) and at the mouth of the bay (Figure 15 and Figure 16). The  
535 ensemble spread of salinity is smaller at the Nakayama Channel (Figure 17), which is similar to  
536 the results of water temperature. Again, there is almost no difference in the ensemble spread  
537 between case 2 and case 5 at the No. 3 buoy (Figure 18). Therefore, as with water temperature,  
538 perturbation of the lateral boundary conditions increases the ensemble spread at all water depths,  
539 especially near the bay mouth, and enables the effective assimilation of observed values.

### 540 3.2.3 River discharge forcing

541 Case 6, which does not perturb the river discharge forcing, shows a similar improvement  
542 in the bias and RMSE scores of water temperature from those of case 2 in Nakayama Channel  
543 and at the No. 3 buoy (Figure 4 and Figure 5). However, the bias and RMSE scores of SST are  
544 worse than those of case 2 in the inner part of the bay (Figure 6 and Figure 7). The ensemble  
545 spread of water temperature for case 6 and case 2 show similar trends in Nakayama Channel and  
546 at the No. 3 buoy. This result indicates that the effect of perturbing river discharge forcing is  
547 particularly large near the river mouth and decreases with distance from the river mouth.  
548 Therefore, perturbation of river discharge forcing ensures appropriate assimilation of water  
549 temperature data in the coastal estuary.

550 For salinity, the RMSE score of case 6 is worse than case 2 at the back of bay (Figure  
551 16). Like water temperature, the error of the river boundary conditions has an increasing  
552 influence on salinity with proximity to the river mouth. Moreover, it is necessary to perturb river  
553 discharge forcing to improve the data assimilation results, especially near the river mouth.

## 554 4 Discussion

### 555 4.1 Performance and robustness of data assimilation

556 Previous studies have not examined the long-term applicability of regional data  
557 assimilation methods for coastal estuaries, nor their ability to reflect seasonal fluctuations.  
558 Moreover, although EnKF has been applied to OSSEs, before this study, it had not been applied  
559 to actual observation data from coastal areas. In this study, the proposed EnKF method achieved  
560 stable assimilation results for both water temperature (Figure 2 and Figure 3) and salinity (Figure  
561 9 and Figure 10) throughout the year, and reflected seasonal fluctuations. Thus, the proposed  
562 regional data assimilation method for coastal estuaries exhibits good applicability and  
563 robustness. The assimilation of water temperature (Figure 4 and Figure 5) and salinity (Figure 11  
564 and Figure 12) data contributed to error correction in the vertical direction (i.e., with water  
565 depth). Water temperature was also corrected in the horizontal direction (Figure 6 and Figure  
566 7). This is because the error covariance was appropriately expressed by generating ensembles  
567 using the proposed method of perturbing boundary conditions.

### 568 4.2 Effect of perturbations to boundary conditions

569 In comparison to the open ocean, lateral boundary conditions and river discharge forcing  
570 are relatively more important in a coastal estuary. However, due to inadequate observation data,

571 it is difficult to provide accurate boundary conditions, causing substantial errors in coastal  
572 numerical simulations. Therefore, in this study, a perturbation was applied to the three boundary  
573 conditions. Although the ensemble spread generally tends to degenerate in coastal estuary  
574 modeling, this was avoided by applying perturbations to lateral boundary conditions and river  
575 discharge forcing (Figure 13, Figure 14, Figure 17, and Figure 18). Although perturbations are  
576 often applied to atmospheric forcing in ocean data assimilation methods, this is the first study to  
577 indicate the importance of applying perturbations to lateral boundary conditions and river  
578 discharge forcing in regional data assimilation for a coastal estuary.

579 In this study, the location where the perturbation was applied was examined, and the  
580 magnitude was obtained by error analyses through comparisons with observation data.  
581 According to the data assimilation results, the magnitude of perturbation was qualitatively  
582 appropriate. Therefore, the method of estimating the magnitude of the perturbation (*Appendix A*)  
583 is considered appropriate, and the error estimation method implemented in this study can be used  
584 for general purposes. However, this study did not evaluate the optimal magnitude of the  
585 perturbation; therefore, this should be considered in future work.

586 Vervatis et al. (2021) noted that, in the open ocean, perturbing the wind speed had the  
587 greatest effect on the ensemble spread of water temperature during data assimilation by EnKF,  
588 and that perturbation of other atmospheric forcing conditions (air temperature and sea level  
589 pressure) was less dominant. They also reported that wind uncertainty had a significant impact  
590 on upper ocean uncertainty for both the geostrophic and Ekman components defined by Sverdrup  
591 dynamics. Similarly, in our regional data assimilation for coastal estuaries, perturbation of the air  
592 temperature was also important for the ensemble spread of water temperature (**Figure 13**)  
593 besides wind speed. These results show the difference between open ocean and coastal modeling.  
594 Figure 4 (b) in Vervatis et al. (2021) shows that the ensemble spread caused by perturbation of  
595 the air temperature was large near the coastline (coastal area). Therefore, the effect of air  
596 temperature perturbations cannot be neglected during data assimilation in coastal areas.

#### 597 4.3 Future work

598 The results here, are a crucial first step in regional coastal data assimilation; however,  
599 many issues remain unresolved. Specifically, the correlation of different boundary conditions  
600 was set to be small to avoid unintended accidental correlations. However, we could not confirm  
601 there were no problems with this setting. For example, the lateral boundary conditions of water  
602 temperature and salinity exhibit a certain correlation. Thus, it is necessary to verify the  
603 assimilation when the perturbation is applied according to the correlation obtained from observed  
604 values. Furthermore, the correlation coefficient between the discharge forcing of each river was  
605 set to 1, which is not the true value. Although the correlation for rivers with short distances  
606 between them is close to 1, rivers with long distances between them may require comparison of  
607 the observed river discharge and water temperatures to estimate the correlation coefficient.

608 Abundant observation data are obtained from satellite and in situ observations in coastal  
609 areas. However, the data assimilation method used in this study cannot simultaneously assimilate  
610 more observation data than ensemble members. Therefore, experiments with a greater amount of  
611 ensemble members are required to assimilate large amounts of observational data. Moreover,  
612 system error in this study was assumed to be constant, regardless of the time or season, and the  
613 perturbations (standard deviation  $\zeta$ ) of boundary conditions were set to constant values.  
614 Therefore, future research should examine whether the proposed data assimilation method is

615 suitable for detailed event analysis (e.g., strong winds, large-scale floods, water mass intrusion  
616 from the open ocean to the inner bay) where the model error, not the boundary conditions, has a  
617 significant effect.

618 Furthermore, confirmation of the reproducibility of salinity data was limited to a  
619 comparison of bias and RMSE scores using in situ observations, and the reproducibility of  
620 salinity distributions was not discussed. However, a method for calculating the highly accurate  
621 planar distribution of coastal areas using satellite observations has recently been developed  
622 (Nakada et al., 2018), which will be used to conduct salinity reproducibility analyses in future  
623 works.

624 Finally, instead of relying on data assimilation, it is also necessary to improve the  
625 simulation model. For example, the salinity bias is reversed between the surface and bottom  
626 layers in this study, which may be because the salinity of the model output is less diffused in the  
627 vertical direction than in reality. As the positive and negative biases are the same in the data  
628 assimilation results (Figure 11 and Figure 15), it is necessary to modify the simulation model to  
629 consider diffusion in the vertical direction.

#### 630 **4 Conclusions**

631 Despite previous numerical experiments of data assimilation (OSSEs), this is the first  
632 study to apply the EnKF to regional data assimilation of coastal estuaries using actual long-term  
633 observation data. Specifically, data assimilation was performed for water temperature and  
634 salinity. According to comparisons with observation data not used in the assimilation, the  
635 simulated water temperature and salinity data were corrected in the horizontal and vertical  
636 directions (i.e., with water depth). In addition, the proposed method achieved stable long-term  
637 data assimilation over one year and responded to seasonal fluctuations. Besides perturbations to  
638 atmospheric forcing adopted in previous open ocean data assimilation, model accuracy scores,  
639 and the ensemble spread of water temperature and salinity revealed that perturbations of the  
640 lateral boundary conditions and river discharge forcing are important for regional data  
641 assimilation in coastal estuaries.

#### 642 **Acknowledgments**

643 This study results from commissioned research from Chubu Regional Bureau, Ministry of  
644 Land, Infrastructure, Transport, and Tourism, Japan. This work was supported by JSPS  
645 KAKENHI Grant Number 21K14255. Observed data were obtained from Chubu Regional  
646 Bureau, Ministry of Land, Infrastructure, Transport, and Tourism of Japan, the Japan  
647 Meteorological Agency, Aichi Fisheries Research Institute, and the National Oceanic and  
648 Atmospheric Administration (NOAA). We extend thanks to Shun Ohishi and Teruhisa Okada for  
649 their advice on our study. We would like to thank Editage ([www.editage.com](http://www.editage.com)) for the English  
650 language editing. No potential conflict of interest was reported by the authors.

651

#### 652 **References**

653 Anderson, J. L., & Anderson, S. L. (1999). A Monte Carlo implementation of the nonlinear  
654 filtering problem to produce ensemble assimilations and forecasts. *Monthly Weather Review*,  
655 *127*(12), 2741–2758. [https://doi.org/10.1175/1520-0493\(1999\)127<2741:AMCIOT>2.0.CO;2](https://doi.org/10.1175/1520-0493(1999)127<2741:AMCIOT>2.0.CO;2)

- 656 Baduru, B., Paul, B., Banerjee, D. S., Sanikommu, S., & Paul, A. (2019). Ensemble based  
657 regional ocean data assimilation system for the Indian Ocean: Implementation and evaluation.  
658 *Ocean Modelling*, 143. <https://doi.org/10.1016/j.ocemod.2019.101470>
- 659 Bougeault, P., Toth, Z., Bishop, C., Brown, B., Burridge, D., Chen, D. H., et al. (2010). The  
660 THORPEX Interactive Grand Global Ensemble. *Bulletin of the American Meteorological*  
661 *Society*, 91(8), 1059–1072. <https://doi.org/10.1175/2010BAMS2853.1>
- 662 Brankart, J.-M., Candille, G., Garnier, F., Calone, C., Melet, A., Bouttier, P.-A., et al. (2015). A  
663 generic approach to explicit simulation of uncertainty in the NEMO ocean model. *Geoscientific*  
664 *Model Development*, 8(5), 1285–1297. <https://doi.org/10.5194/gmd-8-1285-2015>
- 665 Edwards, C. A., Moore, A. M., Hoteit, I., & Cornuelle, B. D. (2015). Regional ocean data  
666 assimilation. *Annual Review of Marine Science*, 7(1), 21–42. [https://doi.org/10.1146/annurev-](https://doi.org/10.1146/annurev-marine-010814-015821)  
667 [marine-010814-015821](https://doi.org/10.1146/annurev-marine-010814-015821)
- 668 Evensen, G. (1994). Sequential data assimilation with a nonlinear quasi-geostrophic model using  
669 Monte Carlo methods to forecast error statistics. *Journal of Geophysical Research*, 99(C5),  
670 10143. <https://doi.org/10.1029/94JC00572>
- 671 Evensen, G. (2003). The Ensemble Kalman Filter: theoretical formulation and practical  
672 implementation. *Ocean Dynamics*, 53(4), 343–367. <https://doi.org/10.1007/s10236-003-0036-9>
- 673 Evensen, G. (2009). *Data assimilation: the Ensemble Kalman Filter* (2. ed). Dordrecht: Springer.
- 674 Fisher, M., & Courtier, P. (1995). Estimating the covariance matrices of analysis and forecast  
675 error in variational data assimilation. ECMWF Technical Memoranda, 220.  
676 <https://doi.org/10.21957/1DXRASJIT>
- 677 Fisher, R. A., & Yates, Frank. (1948). *Statistical tables for biological, agricultural and medical*  
678 *research*. London: Oliver and Boyd.
- 679 Fu, L.-L., Fukumori, I., & Miller, R. N. (1993). Fitting dynamic models to the geosat sea level  
680 observations in the Tropical Pacific Ocean. Part II: A linear, wind-driven model. *Journal of*  
681 *Physical Oceanography*, 23(10), 2162–2181. [https://doi.org/10.1175/1520-](https://doi.org/10.1175/1520-0485(1993)023<2162:FDMTTG>2.0.CO;2)  
682 [0485\(1993\)023<2162:FDMTTG>2.0.CO;2](https://doi.org/10.1175/1520-0485(1993)023<2162:FDMTTG>2.0.CO;2)
- 683 Gaspari, G., & Cohn, S. E. (1999). Construction of correlation functions in two and three  
684 dimensions. *Quarterly Journal of the Royal Meteorological Society*, 125(554), 723–757.  
685 <https://doi.org/10.1002/qj.49712555417>
- 686 Hafeez, M. A., Nakamura, Y., Suzuki, T., Inoue, T., Matsuzaki, Y., Wang, K., & Moiz, A.  
687 (2021). Integration of Weather Research and Forecasting (WRF) model with regional coastal  
688 ecosystem model to simulate the hypoxic conditions. *Science of The Total Environment*, 771,  
689 145290. <https://doi.org/10.1016/j.scitotenv.2021.145290>
- 690 Hamill, T. M., Whitaker, J. S., & Snyder, C. (2001). Distance-Dependent Filtering of  
691 Background Error Covariance Estimates in an Ensemble Kalman Filter. *Monthly Weather*  
692 *Review*, 129(11), 2776–2790. [https://doi.org/10.1175/1520-](https://doi.org/10.1175/1520-0493(2001)129<2776:DDFOBE>2.0.CO;2)  
693 [0493\(2001\)129<2776:DDFOBE>2.0.CO;2](https://doi.org/10.1175/1520-0493(2001)129<2776:DDFOBE>2.0.CO;2)
- 694 Henderson-Sellers, B. (1985). New formulation of eddy diffusion thermocline models. *Applied*  
695 *Mathematical Modelling*, 9(6), 441–446. [https://doi.org/10.1016/0307-904X\(85\)90110-6](https://doi.org/10.1016/0307-904X(85)90110-6)
- 696 Hoffman, M. J., Miyoshi, T., Haine, T. W. N., Ide, K., Brown, C. W., & Murtugudde, R. (2012).  
697 An advanced data assimilation system for the Chesapeake Bay: Performance evaluation. *Journal*  
698 *of Atmospheric and Oceanic Technology*, 29(10), 1542–1557. [https://doi.org/10.1175/JTECH-D-](https://doi.org/10.1175/JTECH-D-11-00126.1)  
699 [11-00126.1](https://doi.org/10.1175/JTECH-D-11-00126.1)
- 700 <https://doi.org/10.1175/JTECH-D-11-00126.1>

- 701 Hoteit, I., Luo, X., Bocquet, M., Köhl, A., & Ait-El-Fquih, B. (2018). Data assimilation in  
702 oceanography: Current status and new directions. In E. P. Chassignet, A. Pascual, J. Tintoré, & J.  
703 Verron (Eds.), *New Frontiers in Operational Oceanography*. GODAE OceanView.  
704 <https://doi.org/10.17125/gov2018.ch17>
- 705 Khanarmuei, M., Mardani, N., Suara, K., Sumihar, J., Sidle, R. C., McCallum, A., & Brown, R.  
706 J. (2021). Assessment of an ensemble-based data assimilation system for a shallow estuary.  
707 *Estuarine, Coastal and Shelf Science*, 257. <https://doi.org/10.1016/j.ecss.2021.107389>
- 708 Kunii, M., & Miyoshi, T. (2012). Including Uncertainties of Sea Surface Temperature in an  
709 Ensemble Kalman Filter: A Case Study of Typhoon Sinlaku (2008). *Weather and Forecasting*,  
710 27(6), 1586–1597. <https://doi.org/10.1175/WAF-D-11-00136.1>
- 711 Kuwagata, T., & Kondo, J. (1990). Estimation of aerodynamic roughness at the regional  
712 meteorological stations (AMeDAS) in the central part of Japan. *TENKI*, 37(3), 55–59.
- 713 Kwon, K. M., Choi, B.-J., Lee, S.-H., Kim, Y. H., Seo, G.-H., & Cho, Y.-K. (2016). Effect of  
714 model error representation in the Yellow and East China Sea modeling system based on the  
715 ensemble Kalman filter. *Ocean Dynamics*, 66(2), 263–283. [https://doi.org/10.1007/s10236-015-](https://doi.org/10.1007/s10236-015-0909-8)  
716 0909-8
- 717 Lima, L. N., Pezzi, L. P., Penny, S. G., & Tanajura, C. A. S. (2019). An investigation of ocean  
718 model uncertainties through ensemble forecast experiments in the Southwest Atlantic Ocean.  
719 *Journal of Geophysical Research: Oceans*, 124(1), 432–452.  
720 <https://doi.org/10.1029/2018JC013919>
- 721 Matsuzaki, Y., & Inoue, T. (2020). A Study of Calculation Conditions of Data Assimilation for  
722 Flow Analysis of Closed Waters by Ensemble Kalman Filter. *Technical Note of the Port and*  
723 *Airport Research Institute*, (1367), 35.
- 724 Matsuzaki, Y., Fujiki, T., Kawaguchi, K., Inoue, T., & Iwamoto, T. (2021). Application of the  
725 WRF model to the coastal area at Ise Bay, Japan: evaluation of model output sensitivity to input  
726 data. *Coastal Engineering Journal*, 63(1), 17–31.  
727 <https://doi.org/10.1080/21664250.2020.1830485>
- 728 Mirouze, I., & Storto, A. (2019). Generating atmospheric forcing perturbations for an ocean data  
729 assimilation ensemble. *Tellus A: Dynamic Meteorology and Oceanography*, 71(1), 1624459.  
730 <https://doi.org/10.1080/16000870.2019.1624459>
- 731 Moore, A. M., Arango, H. G., Broquet, G., Powell, B. S., Weaver, A. T., & Zavala-Garay, J.  
732 (2011). The Regional Ocean Modeling System (ROMS) 4-dimensional variational data  
733 assimilation systems. *Progress in Oceanography*, 91(1), 34–49.  
734 <https://doi.org/10.1016/j.pocean.2011.05.004>
- 735 Nakada, S., Kobayashi, S., Hayashi, M., Ishizaka, J., Akiyama, S., Fuchi, M., & Nakajima, M.  
736 (2018). High-resolution surface salinity maps in coastal oceans based on geostationary ocean  
737 color images: quantitative analysis of river plume dynamics. *Journal of Oceanography*, 74(3),  
738 287–304. <https://doi.org/10.1007/s10872-017-0459-4>
- 739 Nakamura, Y., & Hayakawa, N. (1991). Modelling of thermal stratification in lakes and coastal  
740 seas (pp. 227–236). Presented at the IAHS Publication (International Association of  
741 Hydrological Sciences). Retrieved from [https://www.scopus.com/inward/record.uri?eid=2-s2.0-](https://www.scopus.com/inward/record.uri?eid=2-s2.0-0025843997&partnerID=40&md5=7952862f01733aee89cce203e30718ca)  
742 0025843997&partnerID=40&md5=7952862f01733aee89cce203e30718ca
- 743 Nimiya, H., Akasaka, H., & Matsuo, Y. (1996). A method to estimate the hourly downward  
744 atmospheric radiation using AMeDAS data. *The Society of Heating, Air-Conditioning Sanitary*  
745 *Engineers of Japan*, (60), 133–144.

- 746 Nimiya, H., Akasaka, H., Matsuo, Y., & Soga, K. (1997). A method to estimate the hourly solar  
 747 radiation using AMeDAS data Part2-Application to the improved sunshine recorder of  
 748 AMeDAS. *The Society of Heating, Air-Conditioning Sanitary Engineers of Japan*, (65), 53–65.
- 749 Orlanski, I. (1976). A simple boundary condition for unbounded hyperbolic flows. *Journal of*  
 750 *Computational Physics*, 21(3), 251–269. [https://doi.org/10.1016/0021-9991\(76\)90023-1](https://doi.org/10.1016/0021-9991(76)90023-1)
- 751 Penny, S. G., Behringer, D. W., Carton, J. A., & Kalnay, E. (2015). A hybrid global ocean data  
 752 assimilation system at NCEP. *Monthly Weather Review*, 143(11), 4660–4677.  
 753 <https://doi.org/10.1175/MWR-D-14-00376.1>
- 754 Prasad, R. (1967). A nonlinear hydrologic system response model. *Journal of the Hydraulics*  
 755 *Division*, 93(4), 201–222.
- 756 Sakov, P., Counillon, F., Bertino, L., Lisæter, K. A., Oke, P. R., & Korabely, A. (2012).  
 757 TOPAZ4: an ocean-sea ice data assimilation system for the North Atlantic and Arctic. *Ocean*  
 758 *Science*, 8(4), 633–656. <https://doi.org/10.5194/os-8-633-2012>
- 759 Sanikommu, S., Toye, H., Zhan, P., Langodan, S., Krokos, G., Knio, O., & Hoteit, I. (2020).  
 760 Impact of atmospheric and model physics perturbations on a high-resolution ensemble data  
 761 assimilation system of the Red Sea. *Journal of Geophysical Research: Oceans*, 125(8).  
 762 <https://doi.org/10.1029/2019JC015611>
- 763 Stanev, E. V., Schulz-Stellenfleth, J., Staneva, J., Grayek, S., Grashorn, S., Behrens, A., et al.  
 764 (2016). Ocean forecasting for the German Bight: from regional to coastal scales. *Ocean Science*,  
 765 12(5), 1105–1136. <https://doi.org/10.5194/os-12-1105-2016>
- 766 Tanaka, Y., & Suzuki, K. (2010). Development of Non-Hydrostatic Numerical Model for  
 767 Stratified Flow and Upwelling in Estuary and Coastal Areas. *Report of the Port and Airport*  
 768 *Research Institute*, 49(1), 3–26.
- 769 Turner, M., Walker, J., & Oke, P. (2008). Ensemble member generation for sequential data  
 770 assimilation. *Remote Sensing of Environment*, 112(4), 1421–1433.  
 771 <https://doi.org/10.1016/j.rse.2007.02.042>
- 772 Vandenbulcke, L., & Barth, A. (2015). A stochastic operational forecasting system of the Black  
 773 Sea: Technique and validation. *Ocean Modelling*, 93, 7–21.  
 774 <https://doi.org/10.1016/j.ocemod.2015.07.010>
- 775 Vervatis, V. D., De Mey-Frémaux, P., Ayoub, N., Karagiorgos, J., Ghantous, M., Kailas, M., et  
 776 al. (2021). Assessment of a regional physical–biogeochemical stochastic ocean model. Part 1:  
 777 Ensemble generation. *Ocean Modelling*, 160. <https://doi.org/10.1016/j.ocemod.2021.101781>
- 778 Weaver, A., & Courtier, P. (2001). Correlation modelling on the sphere using a generalized  
 779 diffusion equation. *Quarterly Journal of the Royal Meteorological Society*, 127(575), 1815–  
 780 1846. <https://doi.org/10.1002/qj.49712757518>
- 781 Whitaker, J. S., & Hamill, T. M. (2012). Evaluating methods to account for system errors in  
 782 ensemble data assimilation. *Monthly Weather Review*, 140(9), 3078–3089.  
 783 <https://doi.org/10.1175/MWR-D-11-00276.1>
- 784 World Meteorological Organization. (2008). *Guide to meteorological instruments and methods*  
 785 *of observation*. Geneva, Switzerland: World Meteorological Organization.

786

787 **Appendix**788 **A. Estimation of the magnitude of perturbation to boundary conditions**789 **A.1 Air temperature**

790 The dominant error factors of the atmospheric forcing condition of air temperature were  
791 the differences between observation points (sea and ground) and the influence of spatial  
792 interpolation. Therefore, it is assumed that the air temperatures are accurate at five locations in  
793 Ise Bay (center of the bay, mouth of the bay, and buoys 1 to 3), where the observed air  
794 temperature is shown in **Table 2**, and from April 2015 to December 2019. The boundary  
795 condition between the air temperature observed at the monitoring locations in Ise Bay and the air  
796 temperature calculated at the same position was extracted every hour. The cumulative frequency  
797 distribution of the absolute difference between the observed value and the calculated value was  
798 obtained after subtracting the average error, and the temperature at which the cumulative  
799 frequency was 68.2% was calculated as 3.05 °C. Therefore, we added system noise with a  
800 normal distribution and a standard deviation of the  $\zeta$  value of 3.05 °C to the boundary conditions  
801 of air temperature for each ensemble member.

802 **A.2 Wind speed**

803 The error factor and  $\zeta$  of the atmospheric forcing condition of wind speed was estimated  
804 using the same method as that for air temperature. The cumulative frequency distribution of the  
805 absolute difference between the observed value and the boundary condition was obtained, and  
806 the value at which the cumulative frequency was 68.2% was calculated as 3.45 m s<sup>-1</sup>. Therefore,  
807 we added system noise with a normal distribution and a standard deviation of the  $\zeta$  value of 3.45  
808 m s<sup>-1</sup> to the boundary conditions of wind speed for each ensemble member.

809 **A.3 Water temperature of the lateral boundary**

810 The error factor of the lateral boundary condition of water temperature was mainly  
811 caused because the original data used to create the boundary conditions was not observed during  
812 the simulation period, but was the average value over 10 years, as explained in section 2.2. Then,  
813  $\zeta$  was estimated as follows. First, it was assumed that the observed water temperature is accurate.  
814 Second, the error was estimated by comparing the observed values with the open boundary  
815 conditions. The comparison period was for one year (2015). The cumulative frequency  
816 distribution of the absolute difference between the observed value and the boundary condition  
817 was calculated after subtracting the average error, and the value at which the cumulative  
818 frequency was 68.2% was calculated as 0.73 °C. Therefore, we added system noise with a  
819 normal distribution and a standard deviation of the  $\zeta$  value of 0.73 °C to the open boundary  
820 condition of water temperature for each ensemble member.

821 **A.4 Salinity of the lateral boundary**

822 The error factor and  $\zeta$  of the lateral boundary condition of salinity was estimated using  
823 the same method as that for water temperature. The cumulative frequency distribution of the  
824 absolute difference between the observed value and the boundary condition was obtained, and  
825 the value at which the cumulative frequency was 68.2% was calculated as 0.20. Therefore, we

826 added system noise with a normal distribution and a standard deviation of the  $\zeta$  value of 0.20 to  
827 the boundary conditions of salinity for each ensemble member.

#### 828 A.5 River discharge

829 The error factors of river discharge were predominantly the estimation error of the  
830 storage function method and the spatiotemporal error of input precipitation. Thus, the  $\zeta$  value of  
831 river discharge was estimated as follows. It was assumed that the rate of fluctuation inherent in  
832 river discharge is the same for each river simultaneously. When the rate of discharge fluctuation  
833 varies for each river, the variation is regarded as the error of the river discharge. The analysis  
834 period was set from April 2015 to December 2019, and the average discharge was calculated for  
835 the 10 major rivers flowing into Ise Bay. The river discharge change rate was calculated by  
836 dividing the discharge of each river at each time by the average discharge for each river, and the  
837 standard deviation for each time was obtained. When the cumulative frequency of the standard  
838 deviation was 68.2%, the value was calculated as 0.35. Therefore, the boundary condition was  
839 multiplied by the system noise with a normal distribution and a standard deviation of 0.35.

#### 840 A.6 River water temperature

841 The spatial correlation error and estimation error were considered the dominant error  
842 factors of river water temperature. Therefore, when there was a difference in water temperature  
843 between rivers, system noise was added by assuming that it was an error. The standard deviation  
844 regarding the variation in water temperature at each time for each river was calculated for the 10  
845 major rivers that flow into Ise Bay. The analysis period was from April 2015 to December 2019.  
846 Then, if the distribution of the magnitude of the error for the entire period follows a normal  
847 distribution, the cumulative frequency distribution was created, and the value at which the  
848 cumulative frequency was 68.2% was calculated. Therefore, we added system noise with a  
849 normal distribution and a standard deviation of the  $\zeta$  value of 1.21 °C to the boundary condition  
850 of temperature for each ensemble member.  
851